Gondwana Research 42 (2017) 104–125

Contents lists available at ScienceDirect

Gondwana Research

journal homepage: www.elsevier.com/locate/gr

Hot subduction in the middle Jurassic and partial melting of oceanic crust in Chilean Patagonia

Samuel Angiboust [a,b,*], Thais Hyppolito [c,d], Johannes Glodny [a], Aitor Cambeses [d], Antonio Garcia-Casco [d,e], Mauricio Calderón [f], Caetano Juliani [c]

[a] GFZ German Research Centre for Geosciences, 14473 Potsdam, Germany
[b] Institut de Physique du Globe de Paris, Sorbonne Paris Cité, Univ. Paris Diderot, CNRS, F-75005 Paris, France
[c] Instituto de Geociências, Rua do Lago, 562, Universidade de São Paulo, 05505-080 São Paulo, Brazil
[d] Facultad de Ciencias, Universidad de Granada, Fuentenueva s/n, 18071 Granada, Spain
[e] Andalusian Institute of Earth Sciences, CSIC-Univ. Granada, Spain
[f] Carrera de Geología, Universidad Andres Bello, Sazie 2119, Santiago, Chile

ARTICLE INFO

Article history:
Received 15 August 2016
Received in revised form 19 October 2016
Accepted 22 October 2016
Available online 27 October 2016

Keywords:
Hot subduction
Patagonia
Counter-clockwise P-T path
Trondhjemite
Jurassic

ABSTRACT

Rare remnants of a Mesozoic subduction high pressure (HP) accretionary complex are exposed on Diego de Almagro Island in Chilean Patagonia. We herein focus on the Lazaro unit, a coherent slice of oceanic crust exposed on this island that has been first affected by high temperature (HT) metamorphism followed by a lower temperature deformation event (LT). Its Pressure-Temperature-time (P-T-t) evolution is reconstructed using field and petrographic observations, phase relations, thermobarometry and geochronology. Remnants of a primary amphibolite to HP granulite-facies event in mafic rocks comprising garnet (with ilmenite exsolutions), diopside, trondhjemitic melt, pargasite, plagioclase ± epidote are reported for the first time in neosomes, indicating peak P-T conditions of 1.1–1.3 GPa and c. 750 °C. This peak T paragenesis has been thoroughly overprinted by a phengite-chlorite-actinolite assemblage during isobaric cooling down to c. 450 °C. U-Pb dating of zircon metamorphic rims from a metasedimentary rock yielded a homogeneous age population of 162 ± 2 Ma for the HT event. Sm-Nd dating of two peritectic garnet-bearing samples yield ages of 163 ± 2 Ma and 163 ± 18 Ma for the HT event. Multi-mineral Rb-Sr dating of a metasedimentary rock overprinted by LT deformation suggests retrograde shearing between 120 and 80 Ma. Our results show that the HT event in the Lazaro unit took place at around 160–165 Ma, shortly before the onset of Patagonian Batholith emplacement. Partial melting of subducted oceanic crust reported in the Lazaro unit is related to the early stages of hot subduction along the Gondwana western margin. The Lazaro unit remained at c. 40 km depth along the subduction interface for >80 Ma, recording the deformation and long-term cooling of the subduction channel environment until the upper Cretaceous.

1. Introduction

During the consumption of oceanic lithosphere, fluids and melts from the lower plate are transferred to the upper plate, leading to partial melting of the ultramafic wedge and the formation of volcanic arcs, ultimately contributing to the chemical differentiation of the Earth (Tatsumi and Eggins, 1995). Mass transfer processes across the subduction interface have been extensively studied via geochemical, petrological and geophysical investigations (Peacock et al., 1994; Oncken et al., 2003; Maruyama et al., 2009; Spandler and Pirard, 2013; Schmidt and Poli, 2014). Although subject to contamination during migration through the upper plate, arc magmas and volcanic rocks yield valuable information on chemical differentiation and volatile transport highlighting the contribution of various lithological compounds to the melting process (e.g. Plank and Langmuir, 1993; Walowski et al., 2015). Furthermore, high pressure rocks and exhumed former subduction interfaces have the potential to provide in situ insights into natural processes taking place within the mantle wedge region and beneath volcanic arcs (e.g. Hermann et al., 2006; John et al., 2012).

Only a few natural examples documenting partial melting processes and trondhjemite-tonalite genesis in oceanic subduction zones have been reported (e.g. Catalina Schists: Sorensen and Barton, 1987; Cuba mélanges: García-Casco et al., 2008, Lázaro and García-Casco, 2008; N. Iran: Rossetti et al., 2010). The apparent scarcity of such occurrences can be explained by the rarity of material exhumed from sub-arc depths (>100 km) where temperatures are high enough (>700 °C) to enable partial melting of the oceanic crust along normal subduction gradients (e.g. Syracuse et al., 2010). Known occurrences of melt-bearing, exhumed oceanic crust localities correspond to shallower rocks subducted

* Corresponding author.
E-mail addresses: angiboust@ipgp.fr (S. Angiboust), thahyppolito@gmail.com (T. Hyppolito), glodnyj@gfz-potsdam.de (J. Glodny), aitorc@ugr.es (A. Cambeses), agcasco@ugr.es (A. Garcia-Casco), mccaldera@gmail.com (M. Calderón).

http://dx.doi.org/10.1016/j.gr.2016.10.007
1342-937X/

along a hot prograde pressure-temperature (P-T) path (c. 20°/km). Such conditions may have been reached (i) during Archean times (e.g. Van Hunen and Moyen, 2012), (ii) shortly after subduction initiation (e.g. Stern, 2004) or (iii) during subduction of young oceanic lithosphere (e.g. Blanco-Quintero et al., 2011).

We herein report a new occurrence of high-pressure partial melting of subducted oceanic crust on the remote Diego de Almagro Island (Fig. 1; DAI, Chilean Patagonia) and discuss the meaning of this event in the light of new thermobarometric, geochemical and geochronological data. This island represents a unique vestige of a fossil accretionary system developed at the southwestern margin of Gondwana (Hervé and Fanning, 2003; Willner et al., 2004a), where different slices of oceanic crust were underplated between c. 120 Ma and c. 80 Ma and metamorphosed under blueschist to eclogite-facies conditions (Hyppolito et al., 2016). The new results presented here open a window for better understanding the origin of partially molten rocks in this paleo-subduction system and their tectonic significance in a regional context.

2. Geological setting

A very lengthy mountain chain, the Chilean Coastal Cordillera, is exposed almost continuously between latitudes 28° S and 55° S, and includes subduction complexes of Late Paleozoic and Mesozoic ages developed at the southwestern margin of the Gondwana continent via basal and frontal accretionary processes (Hervé, 1988; Glodny et al., 2005; Willner, 2005; Kato and Godoy, 2015). Only three occurrences of albite-epidote amphibolite-facies subduction channel rocks (with counterclockwise P-T paths) have been described along these coastal complexes (Los Pabilos: Willner et al., 2004b; Kato et al., 2008; Punta Sirena: Willner, 2005; Hyppolito et al., 2014; Los Caldos: Willner et al., 2012). South of ca. 46° S, on the western side of the South Patagonian Batholith, isolated exposures of Mesozoic accretionary complexes occur (e.g. Madre de Díos, Diego de Almagro and Diego Ramirez complexes) (e.g. Hervé et al., 2008). Diego de Almagro Island (DAI) is a remote locality (51° 30′ S) close to the Strait of Magellan in Chilean Patagonia (Fig. 1a), which embraces outcrops of Mesozoic metamorphic complexes formed during subduction of the paleo-Pacific ocean beneath the western margin of Gondwana (e.g. Charrier et al., 2007; Hervé et al., 2007; Willner et al., 2004a). To the East of the DAI is exposed the Madre de Díos Accretionary Complex (MDAC), a frontally accreted Triassic actinolite-pumpellyite-facies accretionary prism (Forsythe and Mpodozis, 1979; Hervé et al., 1999; Sepúlveda et al., 2010) where peak metamorphic conditions of ~290–310 °C and 0.4–0.6 GPa have been determined (Willner et al., 2009; Fig. 1a). The DAI is formed by the Cretaceous accretionary Diego de Almagro Metamorphic Complex (DAMC) (Hervé and Fanning, 2003; Willner et al., 2004a; Hyppolito et al., 2016). The MDAC and DAMC, which formed by diachronic tectonic processes, are now separated by a ductile NNW-trending shear zone (the Seno Arcabuz Shear zone: SASZ; Hervé and Fanning, 2003; Olivares et al., 2003; Willner et al., 2004a, 2009). Sinistral strike-slip transport along this shear zone led to partial reworking of the eastern part of the DAI and juxtaposition of the MDAC (Fig. 1b; e.g. Hervé et al., 1999; Olivares et al., 2003; Willner et al., 2009). The main amphibolite-facies deformation event along the SASZ has been estimated from orthogneisses by Willner et al. (2004a) to be around 580–690 °C and 0.5–0.6 GPa. A K-Ar analysis of muscovite yielded an age of 122 ± 4.6 Ma for a garnet mica schist from the SASZ. Willner et al. (2004a) interpreted the HT metamorphism of the SASZ as a consequence of heat advection from the coeval magmatic arc suggesting the formation of a paired belt system in the DAMC (coeval HP-LT and LP-HT belts).

Some DAMC rocks have revealed mid- to late Jurassic protoliths metamorphosed during the early Cretaceous (Hervé et al., 1999; Hervé and Fanning, 2003; Olivares et al., 2003; Willner et al., 2004a). Recent investigations (Hyppolito et al., 2016) have shown that the DAMC is divided into two main parts: the Almagro HP-LT Complex (AC) to the SW and the Lazaro unit to the NE. The Lazaro unit is limited to the E by the SASZ (Fig. 1c). Both the Almagro HP-LT Complex (AC) and the Lazaro unit underwent HP metamorphism and are separated by a major, 50–100 m thick shear zone: the Puerto Shear Zone (PSZ; Fig. 1c; Hervé and Fanning, 2003; Hyppolito et al., 2016). The AC is dominantly composed of N- and E-MORB-type mafic meta-tuffs and meta-pillow lavas with minor intercalations of metasediments (spessartine quartzites and pelitic schists) (Willner et al., 2004a; Hyppolito et al., 2016). Peak pressure metamorphic conditions have been estimated between 1.5 and 1.8 GPa (Hyppolito et al., 2016). Below the PSZ thrust, bodies with relics of eclogite-facies metamorphism with a strong amphibolite-facies overprint (the garnet amphibolite unit) yield multi-mineral Rb-Sr ages of c. 120 Ma (Hyppolito et al., 2016). The garnet amphibolite unit overlies (and is locally tectonically imbricated with) blueschist-facies rocks devoid of an amphibolite-facies overprint that yield much younger Rb-Sr deformation ages of c. 80 Ma (Hyppolito et al., 2016).

The Lazaro unit, on the other hand, has barely been investigated. A few orthogneiss samples have been studied by Hervé et al. (1999),

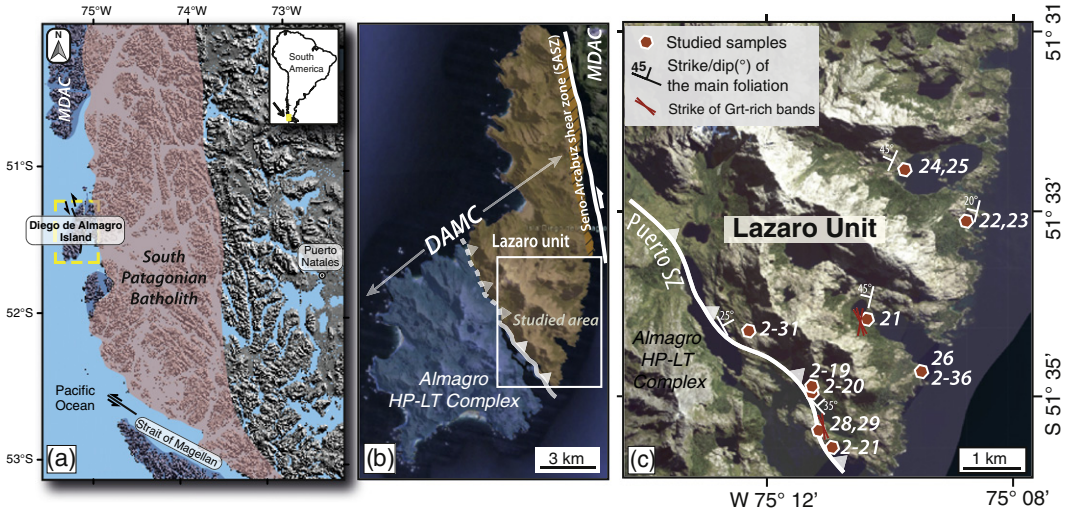

Fig. 1. Geological map of the Lazaro unit. a. Location of Diego de Almagro Island in Chilean Patagonia. b. Simplified geological map of the island showing the main units forming the Diego de Almagro Metamorphic Complex (DAMC) and the Seno Arcabuz Shear Zone (SASZ) that partly reworked the structure in the Lazaro unit (MDAC: Madre de Dios Accretionary Complex). c. Satellite image showing the sampling localities as well as the main structural features.

Hervé and Fanning (2003) and Willner et al. (2004a). These authors noticed that some samples from the Lazaro unit rocks record metamorphism under a relatively warm thermal gradient and also proposed that an orthogneiss body exposed along the SASZ may represent a crustal fragment tectonically eroded from the upper plate that was juxtaposed with HP-LT metamorphic rocks during subduction. The U-Pb age range of 165–170 Ma obtained for zircon rims from a metagranite has been interpreted as a record of pre-subduction extension-related magmatism associated with the break-off of Gondwana during the late Jurasic (Hervé and Fanning, 2003), which culminated with the early development of mafic oceanic-type crust (e.g. the Rocas Verdes basin) at c. 155 Ma (Calderon et al., 2013).

3. Rock types and field relationships of the Lazaro unit

Two field missions focusing on the southern coast of the Diego de Almagro Island were organized in 2007 and 2015. Sampling, petrological observations and structural measurements led to the characterization of the Lazaro unit, a coherent unit forming the eastern and southeastern part of the island where abundant amphibolite and orthogneiss bodies have been reported (Hervé and Fanning, 2003). Our observations, in line with Hervé and Fanning (2003) and Willner et al. (2004a), show that the Lazaro unit has been affected by an early pervasive HT tectono-metamorphic stage followed by a LT overprint. The first HT metamorphic event led to the formation of a subvertical metamorphic foliation striking N–S to NE–SW (Fig. 1c; Electronic Appendix 1). These primary structures are cross-cut by a series of NW-SE striking, greenschist-facies shear zones sub-parallel to the main PSZ structure (Fig. 1c). High Temperature fabrics within the lowermost hundred meters of the Lazaro unit have been transposed along the PSZ leading to the formation of C-S greenschist-facies mylonites as well as rotation-recrystallization of garnet into chlorite. Top-to-NW kinematic indicators as well as evidence of back-shearing have been observed along this thrust contact, which dips 30° to the SE. Similar mylonites are visible in the hanging wall of the underlying Almagro HP-LT Complex, which is also affected by this mylonitization stage.

Evidence for an early high-temperature metamorphic event in the Lazaro unit is attested by the ubiquitous presence of garnet amphibolite and felsic gneiss in all sampling localities (Fig. 1c; Fig. 2a and b). The most frequent rock type in the studied area is a coarse-grained amphibolite with large amounts (>50 vol.%) of dark amphibole crystals between 1 and 3 mm in size. At locality #21 (Fig. 1c) a pluri-hectometric orthogneiss body occurs with coarse-grained intergrowths of hornblende crystals and fibrous epidote that exhibit a pegmatite-like structure (Electronic Appendix 1; see also Willner et al., 2004a, 2004b). At several localities (e.g #25 and #2–31), relics of a garnet-clinopyroxene-plagioclase assemblage suggest that peak metamorphic conditions reached the high pressure granulite facies of Pattison (2003) (stage 1; see Fig. 3a, and petrological results below). All studied localities also exhibit evidence of partial melting of amphibolite with

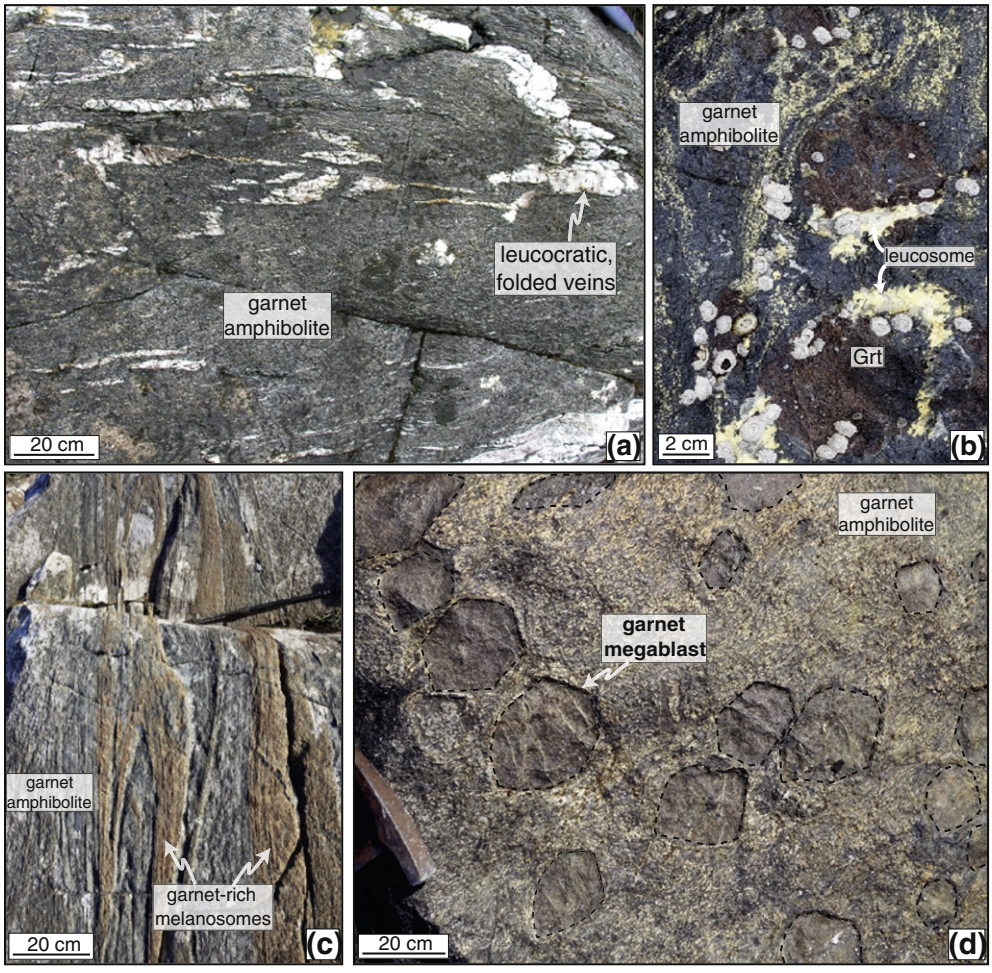

Fig. 2. Field pictures of Lazaro unit exposures. a. Representative Lazaro unit outcrop showing a dark, garnet amphibolite containing numerous decimeter-thick strongly folded leucosomes. b. Coastal exposure of a garnet amphibolite (locality #25) showing 10-cm sized peritectic garnet associated with a yellowish leucosome. c. Representative field view (locality #29) of a garnet amphibolite matrix comprising garnetite layers that can continuously be followed over hundreds of meters. d. Outcrop view of a garnet amphibolite (locality #26) in which garnet megablasts of 15 to 25 cm in diameter can be observed (hammer for scale).

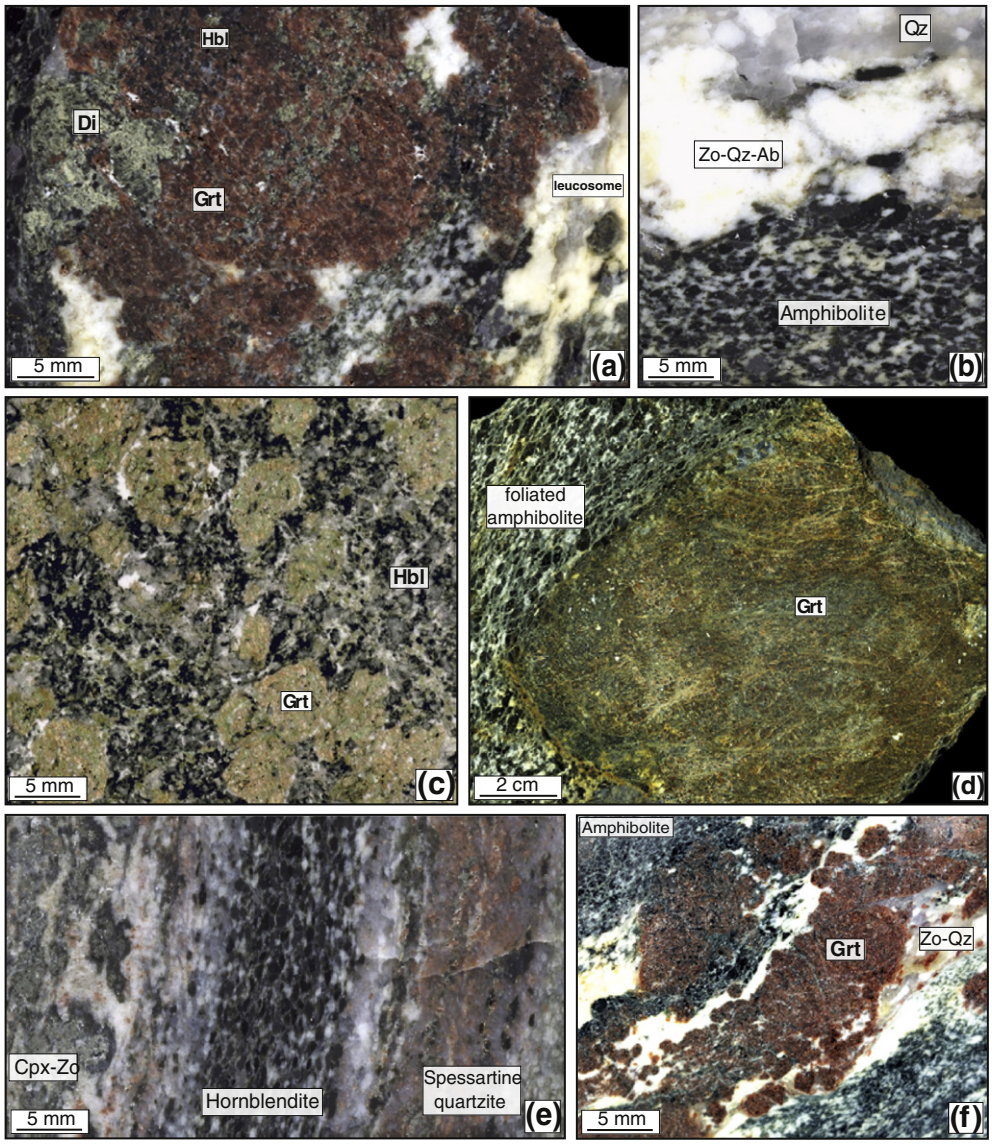

Fig. 3. Hand specimen photos of Lazaro unit HP-HT rocks. a. Polished slab of sample #25 showing a garnet-bearing leucosome comprising peritectic garnet in equilibrium with green diopside and recrystallized melt (mainly formed by quartz and epidote). b. Polished slab of a quartz-epidote-feldspar leucosome cutting through the amphibolite matrix (sample #23). c. Representative view of a sample from a garnetite layer (garnet-bearing residuum) showing high garnet content (>40 vol.%) and abundant hornblende crystals (sample #25c). Note that garnet has been partly replaced by chlorite during cooling. d. Polished section of one of the garnet megablasts shown in picture 2d. This garnet crystal has been wrapped later by an amphibolite-facies matrix (sample #26b). e. Scanned rock slab of a heterogeneous lithological sequence comprising a diopside-epidote assemblage (left), a hornblendite layer (middle) and a pinkish spessartine quartzite (right). This sample (#25a) probably corresponds to a former oceanic volcano-sedimentary rock. f. Polished sample showing the preferential growth of peritectic garnet with quartz-epidote assemblages (former melt) in the middle of an amphibolite (locality #25).

two distinct types of neosomes (following the nomenclature of Sawyer, 2008). Leucosomes contain whitish, cm-sized folded leucocratic bands mainly formed by (saussuritized) plagioclase, quartz, epidote and locally mm-sized titanite crystals (Figs. 2a and 3b). Such leucosomes have been named trondhjemites by Hervé and Fanning (2003). Melanosomes are characterized by garnet, quartz and epidote and local clinopyroxene (Figs. 2b, c and 3c). The proportion of garnet in the melanosomes can be very variable depending on the degree of melt extraction. Some of the garnet bearing melanosomes that contain >50 vol.% garnet are named hereafter garnet-bearing restites (Fig. 3c). The latter form 10 to 50 cm-thick reddish layers that can be continuously tracked over hundreds of meters (Fig. 2c). These networks strike mainly N–S, parallel to the HT fabric, in the two localities where they have been identified (Fig. 1c). At sampling locality #26, several boulders on the seashore exhibit very large, facetted euhedral garnet megablasts (up to 20 cm in diameter) within an amphibolite facies matrix (Figs. 2d and 3d).

Importantly, our field observations revealed the presence of felsic gneiss derived from metasedimentary rocks within the Lazaro unit, interleaved with hornblende-bearing mafic lithologies (Electronic Appendix 1). These rocks are very retrogressed and now characterized by a large amount of quartz, white mica and, to a lesser extent, hornblende porphyroblasts (e.g., sample #24). Two distinct sampling localities (#22 and #25) also exhibit cm-thick silica-rich layers interbedded with amphibolites and containing numerous garnet crystals that give the rock a reddish appearance (Fig. 3e). This texture recalls coticules (spessartine quartzites) reported in various localities along the Chilean paleo-accretionary wedge as well as within the underlying blueschist-facies Almagro Complex (Willner et al., 2001; Hyppolito et al., 2016).

We finally remark that (i) the Lazaro unit comprises an alternation of decameter-thick metasedimentary layers interbedded within mafic lithologies, (ii) partial melting products are restricted to meter to decameter-thick leucosomes, and (iii) mantle lithologies (e.g. peridotite, serpentinite) are lacking in the studied area.

4. Analytical methods

Petrological study has been performed on a set of 20 representative samples located on Fig. 1c. Electron probe microanalyses were performed at the GFZ Potsdam with a JEOL-JXA 8230 probe under common analytical conditions (15 kV, 20 nA, wavelength-dispersive spectroscopy mode), using a 10 μm beam. Standards used for the calibration as follows: orthoclase (Al, Si, K), fluorite (F), rutile (Ti), Cr_2O_3 (Cr), wollastonite (Ca), tugtupite (Cl), albite (Na), MgO (Mg), Fe_2O_3 (Fe) and rhodonite (Mn). Table 1 offers selected analyses of major phases. Elemental XR maps were obtained with the same machine and with a CAMECA SX-100 microprobe (Center of Scientific Facilities of the University of Granada), using albite (Na), periclase (Mg), SiO_2 (Si), Al_2O_3 (Al), sanidine (K), Fe_2O_3 (Fe), $MnTiO_3$ (Mn), SO_4Ba

Table 1
Representative minerals analyses for both stage 1 (HT) and stage 2 parageneses (LT).

Sample	2-21d	2-21d	#22	Sample	#25A	#25	#25A	Sample	#25A	Sample	2-36D	#21A1	Sample	#24	#25A	Sample	#27
Label	Amp	Amp	Amp	Label	Px	Px	Px	Label	Zo1	Label	Core	Core	Label	White mica	White mica	Label	Fsp
Class.	Par	Par	Par	Class.	Di	Di	Di	Class.	Ep	Class.	Grt	Grt	Class.	Ms	Ms	Class.	Olig.
Point	1549	1552	5494	Point	5306	5338	5382	Point	5296	Point	667	5024	Point	5457	5312	Point	6377
Stage	HT	HT	HT	Stage	HT	HT	HT	Stage	HT	Stage	HT	HT	Stage	HT	HT	Stage	HT
SiO_2	42.39	42.78	41.75	SiO_2	52.22	49.46	50.92	SiO_2	37.98	SiO_2	39.25	38.16	SiO_2	44.99	45.26	SiO_2	62.38
TiO_2	0.74	0.76	0.85	TiO_2	0.18	0.25	0.16	TiO_2	0.03	TiO_2	0.09	0.07	TiO_2	0.51	0.00	TiO_2	0.01
Al_2O_3	14.61	14.05	12.97	Al_2O_3	3.34	2.02	2.58	Al_2O_3	29.15	Al_2O_3	22.27	21.33	Al_2O_3	35.81	37.82	Al_2O_3	22.97
FeOt	15.68	15.14	18.73	FeOt	13.31	15.88	19.88	Fe_2O_3	7.23	FeOt	25.00	25.49	FeOt	1.29	0.93	Fe_2O_3	0.26
MnO	0.10	0.12	0.64	MnO	0.40	0.24	0.39	MnO	0.17	MnO	0.73	0.92	MnO	0.00	0.05	CaO	4.91
MgO	9.19	9.56	9.32	MgO	15.75	9.92	12.51	MgO	0.06	MgO	7.85	7.34	MgO	0.81	0.44	Na_2O	8.80
CaO	10.97	11.07	11.51	CaO	13.42	20.92	12.28	CaO	23.99	CaO	6.39	6.96	CaO	0.00	0.07	K_2O	0.03
Na_2O	2.48	2.42	1.68	Na_2O	0.42	0.46	0.29	Total	98.62	Total	101.58	100.27	BaO	0.36	0.18	Total	99.36
K_2O	0.50	0.62	1.19	K_2O	0.10	0.06	0.19	Si	2.94	Si	2.97	2.94	Na_2O	1.05	1.34	Si	2.78
Total	96.67	96.61	98.64	Total	99.14	99.21	99.29	Ti	0.00	Ti	0.01	0.00	K_2O	9.48	8.88	Ti	0.00
Si	6.35	6.41	6.22	Si	1.95	1.91	1.96	Al	2.66	Al	1.99	1.94	Total	94.34	94.96	Al	1.21
Al	2.58	2.48	2.28	Ti	0.01	0.01	0.00	Fe^{3+}	0.42	Fe^{3+}	0.06	0.18	Si	3.03	3.00	Fe^{3+}	0.01
Ti	0.08	0.09	0.10	Al	0.15	0.09	0.12	Mn	0.01	Fe^{2+}	1.52	1.46	Ti	0.03	0.00	Ca	0.23
Fe^{3+}	0.14	0.09	0.56	Fe^{3+}	0.00	0.12	0.00	Mg	0.01	Mn	0.05	0.06	Al	2.84	2.95	Na	0.76
Fe^{2+}	1.82	1.80	1.78	Fe^{2+}	0.42	0.40	0.64	Ca	1.99	Mg	0.89	0.84	Fe^{2+}	0.07	0.05	K	0.00
Mg	2.05	2.14	2.07	Mn	0.01	0.0.1	0.01	XCz	0.86	Ca	0.52	0.57	Mn	0.00	0.00	XAb	0.76
Mn	0.01	0.01	0.08	Mg	0.88	0.57	0.72	XPs	0.14	mg#	0.37	0.37	Mg	0.08	0.04	XAn	0.24
Ca	1.76	1.78	1.84	Ca	0.54	0.86	0.51			XAlm	0.51	0.50	Ca	0.00	0.00	XOr	0.00
NaB	0.20	0.20	0.09	Na	0.03	0.03	0.02			XPyp	0.30	0.29	Ba	0.01	0.00		
NaA	0.52	0.51	0.40	K	0.00	0.00	0.01			XGrs	0.17	0.20	Na	0.14	0.17		
K	0.10	0.12	0.23	mg#	0.68	0.59	0.53			XSps	0.02	0.02	K	0.81	0.75		
sumA	0.62	0.63	0.63	q	96.8	96.4	97.7						mg#	0.53	0.46		
mg#	0.53	0.54	0.54	Jd	3.2	1.6	2.3										
				Acm	0.0	2.0	0.0										
				Na/Na + Ca	0.1	0.0	0.0										
				Jd	0.02	0.03	0.02										
				CaTs	0.03	0.08	0.03										
				Di	0.64	0.52	0.51										
				Hd	0.30	0.36	0.45										

Sample	#28	#29	Sample	#25A	Sample	#25A	#25A	Sample	#25A	#22	Sample	#25C	#25A
Label	Amp	Amp	Label	Zo2	Label	Grt	Grt	Label	White mica	White mica	Label	Fsp	Fsp
Class.	Act	Act	Class.	Ep	Class.	Grt	Grt	Class.	Phg	Phg	Class.	Ab	Ab
Point	5185	5186	Point	5298	Point	5728	5733	Point	5302	5504	Point	5090	5297
Stage	LT	LT	Stage	LT	Stage	LT	LT	Stage	LT	LT	Stage	LT	LT
SiO_2	53.80	53.01	SiO_2	37.82	SiO_2	37.08	36.84	SiO_2	48.07	50.38	SiO_2	67.83	65.64
TiO_2	0.08	0.05	TiO_2	0.00	TiO_2	0.04	0.09	TiO_2	0.06	0.23	TiO_2	0.00	0.00
Al_2O_3	2.60	2.74	Al_2O_3	26.47	Al_2O_3	20.11	19.82	Al_2O_3	27.37	25.57	Al_2O_3	20.56	20.43
FeOt	16.15	16.24	Fe_2O_3	10.51	FeOt	21.20	22.41	FeOt	4.56	4.66	Fe_2O_3	0.24	0.48
MnO	0.25	0.27	MnO	0.15	MnO	7.15	5.22	MnO	0.07	0.07	CaO	0.32	1.80
MgO	13.15	13.43	MgO	0.01	MgO	1.76	2.35	MgO	2.95	3.27	Na_2O	11.89	10.88
CaO	11.39	11.11	CaO	23.44	CaO	12.17	12.58	CaO	0.07	0.02	K_2O	0.05	0.06
Na_2O	0.85	1.09	Total	97.38	Total	99.62	99.46	BaO	0.32	0.24	Total	100.91	99.32
K_2O	0.13	0.14	Si	2.96	Si	2.96	2.93	Na_2O	0.13	0.10	Si	2.93	2.89
Total	98.39	98.07	Ti	0.00	Ti	0.00	0.01	K_2O	10.67	10.76	Ti	0.00	0.00
Si	7.77	7.69	Al	2.44	Al	1.89	1.86	Total	94.33	95.32	Al	1.05	1.06
Al	0.44	0.47	Fe^{3+}	0.62	Fe^{3+}	0.19	0.26	Si	3.30	3.42	Fe^{3+}	0.01	0.02
Ti	0.01	0.01	Mn	0.01	Fe^{2+}	1.23	1.23	Ti	0.00	0.01	Ca	0.01	0.08
Fe^{3+}	0.12	0.23	Mg	0.00	Mn	0.48	0.35	Al	2.22	2.04	Na	0.99	0.93
Fe^{2+}	1.83	1.74	Ca	1.97	Mg	0.21	0.28	Fe^{2+}	0.26	0.26	K	0.00	0.00
Mg	2.83	2.90	XCz	0.80	Ca	1.04	1.07	Mn	0.00	0.00	XAb	0.98	0.91
Mn	0.03	0.03	XPs	0.20	mg#	0.15	0.18	Mg	0.30	0.33	XAn	0.01	0.08
Ca	1.76	1.73			XAlm	0.41	0.42	Ca	0.00	0.00	XOr	0.00	0.00
NaB	0.20	0.21			XPyp	0.07	0.10	Ba	0.01	0.01			
NaA	0.04	0.10			XGrs	0.35	0.37	Na	0.02	0.01			
K	0.02	0.03			XSps	0.16	0.12	K	0.94	0.93			
sumA	0.06	0.12						mg#	0.54	0.56			

(Ba), Cr_2O_3 (Cr), diopside (Ca), TiO_2 (Ti) and vanadinite (Cl) as calibration standards. The images were processed with the software DWImager (Torres-Roldán and García-Casco, unpublished) (Fig. 6). To highlight the minerals and textures of interest, other mineral phases were masked out, and the color images of the phases of interest were overlain onto a grayscale image base-layer calculated with the expression $\sum$ [a.p.f.u./nA/s)i *Ai, (where A is the atomic number and i corresponds to Si, Ti, Al, Fe, Mn, Mg, Ca, Na, Ba, K, P, F and Cl) that contains the basic textural information of the scanned areas. Ternary phase diagrams were calculated using the software CSpace (Torres-Roldan et al., 2000).

Amphibole compositions were normalized following the scheme of Leake et al. (1997) with Fe^{3+} estimated using the average normalization-factor. Chlorite and white mica were normalized to 28 and 11 oxygens, respectively, assuming $Fe_{total} = Fe^{2+}$. Garnet and clinopyroxene compositions were normalized to 12 oxygens and 8 cations and to 6 oxygens and 4 cations, respectively, with Fe^{3+} estimated by stoichiometry. Plagioclase, epidote and titanite were normalized to 8, 12.5 and 5 oxygens, respectively, assuming Fe_{total} as Fe^{3+}. Mineral abbreviations used in this work are after Whitney and Evans (2010).

Major elements (and some trace elements) were analyzed at GFZ Potsdam by X-ray fluorescence (XRF) prepared as fused discs of Li tetraborate-metaborate (FLUXANA FX-×65, sample-to-flux ratio 1:6), and at ACME Analytical Laboratory (Vancouver, Canada) Ltd., where lithium metaborate fusion and XRF spectrometry were also used. The trace elements were analyzed at GFZ Potsdam and ACME Analytical Laboratory by inductively coupled plasma mass spectroscopy (ICP-MS) after lithium metaborate/tetraborate fusion and nitric acid digestion of 0.2 g of the sample. Loss on ignition was determined gravimetrically after heating the sample powder to 1050 °C for 1 h. The analyses are given in Table 2.

In order to provide age constraints for the timing of ductile deformation of the Lazaro unit, we investigated Rb-Sr multi-mineral isotope systematics in samples of white mica-bearing mylonites. Isotopic data was obtained at GFZ Potsdam using a Thermo Scientific TRITON thermal-ionization mass spectrometer. Rb isotope dilution analysis was done in static multicollection mode, and Sr isotopic compositions were measured in dynamic multicollection mode. Standard errors for age calculation of ±0.005% for $^{87}Sr/^{86}Sr$ and ±1.5% for $^{87}Rb/^{86}Sr$ ratios have been assigned to the results, provided that individual analytical uncertainties were smaller than these values. Mineral separates handling and analytical procedures are described in detail in Glodny et al. (2008). Uncertainties of isotope and age data are quoted at the 2σ level. The program ISOPLOT/EX 3.71 (Ludwig, 2009) was used to calculate regression lines. We used the Rb decay constants recommended by Villa et al. (2015).

For the Sm-Nd work, minerals were recovered from small (~50 g) rock fragments using a roll mill for crushing, followed by heavy liquid and magnetic separation techniques. Garnet separates were purified by treatment in 6 N HCl in an ultrasonic bath in order to remove adherent apatite. All mineral separates including garnet, apatite, amphibole, titanite and feldspar were finally handpicked under a binocular microscope.

Sm-Nd isotopic data were generated at GFZ Potsdam using a Thermo Scientific TRITON thermal ionization mass spectrometer. Nd isotopic

Table 2
Bulk-rock compositions of studied samples from the Lazaro unit. (*): analysis made in ACMElabs, Canada. (**): analysis made in GFZ Potsdam, Germany.

Sample	#23**	2-19G*	#22**	#28**	2-36C*	#26B**	2-20C*	#25**	2-21D*	#25C**	2-31B*	#21A1**	2-21C*	#21**	#25B**	#24**
Rock type	Amp.	Amp.	Amp.	Amp	Amp.	Grt Amp	Grt Amp	Di-Grt Amp	Grt Amp	Grt Amp	Di-Grt Amp	Grt Amp	Grt Amp	Peg.	Trondh.	Sedim.
SiO_2 (wt.%)	48.70	48.18	55.54	43.74	44.33	43.79	47.03	45.47	46.01	47.00	44.63	44.08	43.18	44.90	60.92	73.08
TiO_2	1.68	0.95	1.05	2.41	1.94	1.68	1.88	2.44	1.30	1.19	1.72	1.46	1.64	1.54	0.11	0.55
Al_2O_3	14.27	11.21	12.65	13.47	19.00	18.32	14.66	14.28	17.62	22.65	14.80	19.38	15.45	23.01	22.50	14.40
FeO(t)	14.26	14.08	12.09	16.36	10.30	12.50	16.22	17.40	18.77	12.28	19.92	12.16	21.21	8.88	1.27	4.04
MnO	0.19	0.17	0.36	0.20	0.15	0.13	0.27	0.29	0.57	0.22	0.37	0.20	0.52	0.11	0.02	0.06
MgO	7.43	11.25	5.13	11.53	8.44	8.67	5.67	5.05	5.38	2.63	6.04	8.76	7.53	6.66	0.59	1.35
CaO	10.14	11.48	10.57	10.70	14.37	13.54	11.56	12.97	8.19	10.35	12.02	12.99	8.97	14.41	5.76	1.55
Na_2O	2.91	2.32	1.81	0.83	1.21	1.05	2.15	1.16	1.46	2.86	0.30	0.82	0.59	0.33	8.02	2.22
K_2O	0.26	0.33	0.68	0.71	0.06	0.03	0.33	0.70	0.22	0.60	0.04	0.06	0.31	0.13	0.68	2.64
P_2O_5	0.15	0.02	0.12	0.04	0.20	0.30	0.24	0.25	0.49	0.20	0.17	0.09	0.60	0.02	0.13	0.09
LOI	0.41	1.70	2.32	0.75	3.10	4.03	1.00	0.95	1.60	3.60	2.15	4.83	1.70	4.01	0.81	2.55
$Na_2O + K_2O$	3.17	2.66	2.48	1.55	1.28	1.08	2.48	1.86	1.67	3.47	0.34	0.89	0.90	0.46	8.70	4.87
mg#	0.48	0.59	0.43	0.56	0.59	0.55	0.38	0.34	0.34	0.28	0.35	0.56	0.39	0.57	0.45	0.37
Ba (μg/g)	35	30	118	102	17	5.0	45	237	32	93	4	32	38	41	104	485
Rb	5.0	5.9	12	15	0.7	5.0	2.4	13	1.8	23	0.3	5.0	2.3	5.0	12	118
Sr	121	154	86	125	332	311	144	253	178	184	66	340	87	552	96	167
Y	46	18	30	40	3	b.d.l.	41	49	150	33	51	b.d.l.	110	11	4	26
Zr	113	23	64	61	20	26	96	137	382	45	34	29	441	21	14	230
Nb	10.0	1.5	b.d.l	7.6	5.0	b.d.l	7.0	11.9	10.5	10.0	2.2	5.0	13.3	b.d.l	2.2	12.0
Th	1.5	b.d.l.	n.a.	0.2	b.d.l.	n.a.	0.2	1.6	0.8	n.a.	0.2	n.a.	0.7	n.a.	1.9	n.a.
Cu	100	42	n.a.	33	1	n.a.	113	20	6	n.a.	20	n.a.	19	n.a.	6	n.a.
Ni	47	81	67	24	55	31	93	82	24	107	97	30	27	38	21	16
V	379	574	326	1308	457	429	471	482	238	194	534	355	319	457	32	77
Cr	71	226	89	136	171	175	130	121	68	360	103	81	103	180	76	54
Hf	0.9	1.1	n.a.	1.0	0.8	n.a.	3.2	1.5	9.4	n.a.	1.3	n.a.	11.4	n.a.	0.3	n.a.
Sc	51	65	40	126	40	n.a.	55	57	71	46	72	n.a.	92	n.a.	7	27
La	14.5	0.7	7.5	5.3	3.0	n.a.	5.5	12.8	12.2	11.0	3.3	1.2	15.7	4.3	7.1	24.0
Ce	30.5	2.4	15.0	18.9	10.0	n.a.	16.1	30.3	37.8	27.0	11.0	5.0	53.0	11.0	10.8	51.0
Pr	3.9	0.6	2.2	3.6	1.7	n.a.	2.6	4.3	6.2	4.7	1.8	0.9	8.6	1.2	1.1	6.2
Nd	16.9	3.9	10.0	20.4	8.9	n.a.	13.8	20.5	32.7	21.0	9.7	5.1	43.8	5.4	4.1	24.0
Sm	4.5	1.6	3.0	7.0	2.0	n.a.	4.3	6.1	9.2	5.5	3.7	1.4	12.4	1.4	0.9	4.8
Eu	1.5	0.6	0.9	1.5	1.2	n.a.	1.5	2.2	1.5	1.4	1.2	0.8	1.5	0.6	0.6	1.3
Gd	5.3	2.3	3.8	7.2	1.5	n.a.	5.9	7.0	14.4	5.7	6.0	1.5	15.1	1.7	0.8	4.3
Tb	0.9	0.5	0.8	1.2	0.2	n.a.	1.1	1.2	3.2	0.9	1.3	0.2	2.8	0.2	0.1	0.7
Dy	6.1	2.8	4.6	7.5	0.9	n.a.	6.9	8.0	21.9	4.9	8.3	0.9	17.6	1.2	0.6	3.8
Ho	1.4	0.6	1.0	1.5	0.1	n.a.	1.5	1.8	5.5	0.9	1.9	0.2	4.0	0.3	0.1	0.7
Er	3.9	2.1	3.1	4.0	0.3	n.a.	4.5	5.0	17.1	2.8	5.9	0.5	13.1	0.7	0.3	2.3
Tm	0.6	0.3	0.5	0.5	0.0	n.a.	0.7	0.7	3.1	0.4	0.9	0.1	2.1	0.1	0.1	0.3
Yb	3.8	2.2	3.2	3.4	0.3	n.a.	4.2	4.7	20.5	2.6	5.9	0.5	14.5	0.6	0.3	2.3
Lu	0.6	0.3	0.5	0.5	0.0	n.a.	0.6	0.8	3.6	0.4	0.9	0.1	2.3	0.1	0.0	0.4

compositions were measured in dynamic multicollection mode. Nd and Sm concentrations were determined by isotope dilution using a mixed ^{149}Sm-^{150}Nd tracer, and measured in static multicollection mode. The value obtained for $^{143}Nd/^{144}Nd$ in the La Jolla Nd standard prior to analysis of samples was 0.511850 ± 0.000004 ($n = 7$). For age calculation, standard errors of ±0.002% for $^{143}Nd/^{144}Nd$ ratios, and ±0.5% for $^{147}Sm/^{144}Nd$ ratios were assigned to the results, provided that individual analytical uncertainties were smaller than these values. Otherwise, individual analytical uncertainties were used. Uncertainties of isotope and age data are quoted at 2σ throughout this work. The program ISOPLOT/EX 3.71 (Ludwig, 2009) was used to calculate regression lines. Ages quoted here are based on a decay constant $\lambda^{147}Sm = 6.54 \times 10^{-12}$ year^{-1} (Villa et al., 2015).

Two kilograms of metasedimentary rock sample #24 were processed to obtain zircons for dating. The U-Th-Pb SHRIMP zircon analyses were performed at the CIC (Centro de Instrumentación Científica) of the University of Granada. Zircon was separated using panning, first in water and then in ethanol. This was followed by magnetic extraction of Fe-rich minerals with a Nd magnet. Finally, zircons were handpicked using a binocular microscope. The zircons were cast on "megamounts" (i.e., 35 mm epoxy discs) fixed on the front of a mount holder so that no metallic parts or surface discontinuities faced the secondary ions extraction plate. The minerals were carefully studied with optical (reflected and transmitted light) and scanning electronic microscopy (backscattering and cathodoluminescence) prior to SHRIMP analyses with the IBERSIMS SHRIMP IIe/mc ion microprobe.

Zircons were analyzed for U-Th-Pb following the method described by Williams and Claesson (1987). The mount was coated with a c.12 nm thick gold layer. Each spot was rastered with the primary beam for 120 s prior to analysis and then analyzed for 6 scans following the isotope peak sequence $^{196}Zr_2O$, ^{204}Pb, ^{204}Pb background, ^{206}Pb, ^{207}Pb, ^{208}Pb, ^{238}U, ^{248}ThO, ^{254}UO. All peaks of every scan were measured sequentially 10 times with the following total counting times per scan: 2 s for mass 196; 5 s for masses 238, 248, and 254; 15 s for masses 204, 206, and 208; and 20 s for mass 207. The primary oxygen beam was set to an intensity of about 5 nA, with a 120 μm Kohler aperture, which generated 17 × 20 μm elliptical spots on the target. The secondary beam exit slit was fixed at 80 μm, achieving a resolution of about 5000 at 1% peak height. All calibration procedures were performed on the standards included on the same mount. Mass calibration was done on the REG zircon (ca. 2.5 Ga, very high U, Th and common lead content). The analytical session started by measuring the SL13 zircon (Claoue-Long et al., 1995), which was used as a concentration standard (238 μg/g U). The TEMORA zircon (416.8 ± 1.1 Ma; Black et al., 2003), used as an isotope ratios standard, was then measured in between every 4 unknowns. Data reduction was done with the SHRIMPTOOLS software (available from www.ugr.es/~fbea), which is a new implementation of the PRAWN software originally developed for the SHRIMP. Errors are reported at the 95% confidence interval (≈2 σ). Standard errors (95% C·I) on the 37 replicates of the TEMORA standard measured during the analytical session were ±0.35% for $^{206}Pb/^{238}U$ and ±0.83% for $^{207}Pb/^{206}Pb$.

5. Petrology

5.1. Microtextures and mineral chemistry

5.1.1. Garnet amphibolite and garnet-bearing restites

All the 17 mafic samples from the Lazaro unit studied here were variably affected by retrogression and deformation. In the most re-equilibrated samples, the peak T event is nearly erased and the rocks have been transformed into greenschist facies mylonites (e.g. sample #29a; Electronic Appendix 2). Only samples where the HT event is best preserved exhibit rounded diopside crystals included within garnet (Figs. 3a, e and 4a), since matrix diopside is usually pseudomorphed by hornblende (Fig. 4a). When preserved, clinopyroxene is diopside-rich (X_{Di} = 0.51–0.64) with Ca-tschermak contents comprised between 0.02 and 0.10 (see Table 1 for representative analyses).

Amphibole comprises brown to deep greenish crystals with compositions varying between pargasite, edenite and hornblende (Fig. 5). In strongly mylonitized samples hornblende porphyroclasts locally preserve Stage 1 pargasite compositions in the cores as patches, indicating growth of Stage 2 hornblende during cooling after HT conditions (Fig. 5a and b). The compositional zoning is characterized by nearly constant Na_B (~0.25 a.p.f.u.) and decreasing $Na + K_{(A)}$ (~0.70–0.10) (Fig. 5a) suggesting cooling at relatively constant pressure. Hornblende is frequently observed at the rims of diopside (Figs. 4a and 5a, b) or completely replacing former diopside due to the pervasive fracture network affecting garnet crystals. The garnet-diopside peak T assemblage in melanosomes is closely intergrown with leucocratic domains now composed of quartz and a fine-grained mixture of albite and epidote (Figs. 3a, f, 4b and 6a). This mixture defines rounded to quadrangular shapes and exhibits integrated composition roughly corresponding to a Na-Ca plagioclase. Plagioclase is almost systematically replaced by this mixture except one small inclusion in a garnet core with oligoclase composition (An_{24}; Table 1). Fig. 6c shows one former plagioclase inclusion replaced by a Na-rich feldspar included within a garnet crystal that shows enrichment in Grs component ($Grs_{91}Alm_7Sps_2$) around the inclusion, likely by means of the decomposition of the pristine plagioclase (plagioclase = albite + epidote + grossular-rich garnet).

Two generations of epidote have been texturally identified. The first generation (Ps_{10-15}) is tightly intergrown with quartz forming a myrmekite-like texture (cf. Shelley, 1967) around peritectic garnet (see below) within garnet bearing restites (Fig. 6b). The second generation (Ps_{15-25}) is ubiquitous in Lazaro rocks and forms after replacement of Na-Ca plagioclase. It typically exhibits two pseudomorphic habits: (i) fine grained intergrowths of albite and epidote (Fig. 6a), (ii) coarse grained radiating epidote crystals.

We also report the presence of rounded polymineralic inclusions (20–40 μm in diameter) within garnet grains (Fig. 6d). The inclusion shown in Fig. 6d contains albite, titanite, muscovite and chlorite. The size, presence of low-angle boundaries and composition of these inclusions contrast with those of the aforementioned pseudomorphs after plagioclase in garnet. Retrogression-related microfracturing is responsible for retrogression and the growth of LT minerals within the inclusion.

A network of exsolved 2 μm ilmenite and rutile needles are locally present within garnet (Fig. 4c), in particular within megablasts (Fig. 3d). These megablasts also contain numerous, 50–500 μm apatite crystals as well as numerous ilmenite crystals (Fig. 4d). Ilmenite is frequently observed in Lazaro unit garnet amphibolites, locally rimmed by rutile (Fig. 6e). Rutile forms euhedral grains and needles included within pargasite. In sample #25, 100–250 μm titanite porphyroblasts are included within garnet, pargasite cores and leucocratic domains.

Garnet occasionally exhibits some zoning. Garnet I generation (cores) is weakly zoned. It is often rimmed by a variably thick garnet II generation with lower Mg content (typically 0.05–0.15; Fig. 7). Complex networks of healed fractures with much lower XMg compositions and higher Mn and Ca contents are present in garnet II (Figs. 7a, b and c).

Zoned white mica crystals exhibit muscovite cores rich in Ti and Na, in contrast to phengite-rich rims (Si = 3.35–3.4 a.p.f.u.) that developed around them (Fig. 5c, d and e). Biotite is rare and only observed included in garnet or pargasite cores (Table 1).

Mineral assemblages developed during cooling comprise combinations of phengite, chlorite, epidote (Ps_{20-30}), hornblende, actinolite and titanite (Fig. 8). Phengite (Si = 3.4–3.45 a.p.f.u.) is visible along garnet cracks in the least deformed samples and parallel to the foliation in the most sheared samples (Table 1). Chlorite frequently replaces garnet along cracks and also defines the foliation intergrown with phengite flakes. In sample #25c, two chlorite generations (XMg = 0.6 and 0.4) suggest multiple re-equilibration stages during cooling. Actinolite is systematically observed around hornblende crystals (Figs. 5a, b). Titanite replaces ilmenite-rutile aggregates (Fig. 6e). The paragenetic evolution

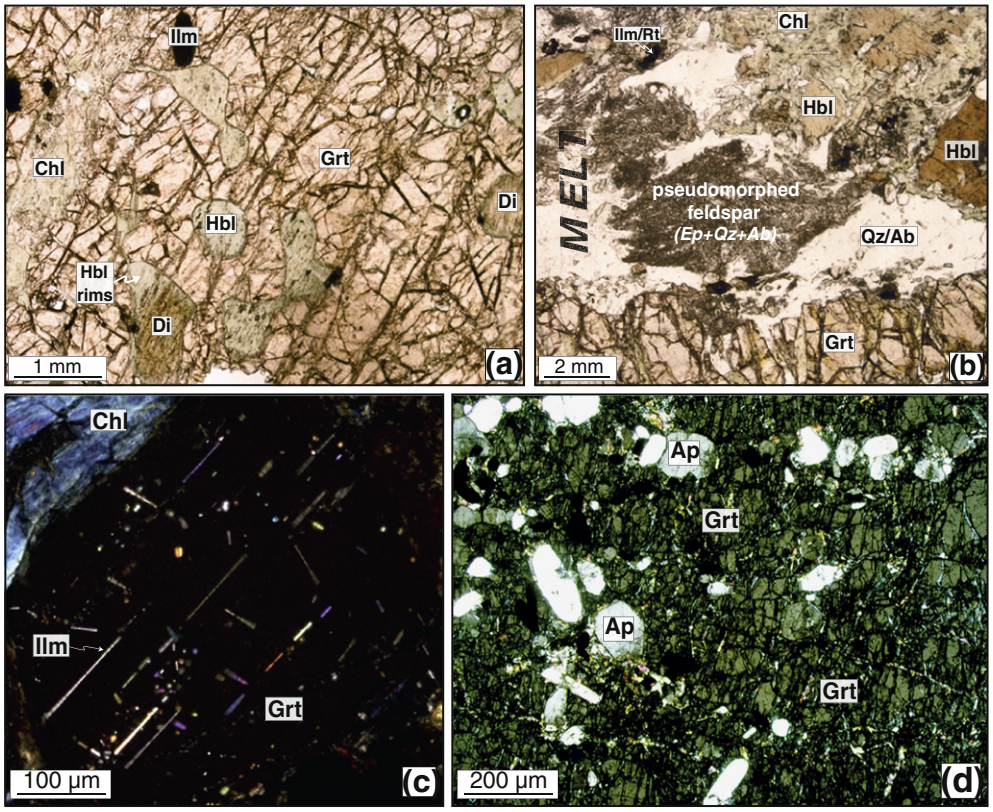

Fig. 4. Optical microscope pictures. a. Rounded diopside inclusions within garnet, partly replaced by hornblende (sample #2–31). Note the strong fracturing of garnet and the partial replacement by chlorite. b. Image showing microtextural relationships between garnet, the leucosome and hornblende (sample #25). Plagioclase crystals are now replaced ('saussuritized') by a fine-grained mixture of albite and zoisite-rich epidote. c. Cross-polarized view of a garnet crystal (sample #26b) showing exsolved ilmenite and rutile needles defining a geometric network. Note that this garnet is compositionally homogeneous (no zoning). d. View showing the abundance of apatite inclusions in the garnet megablast used for Sm-Nd dating (sample #26b; crossed-polarized view).

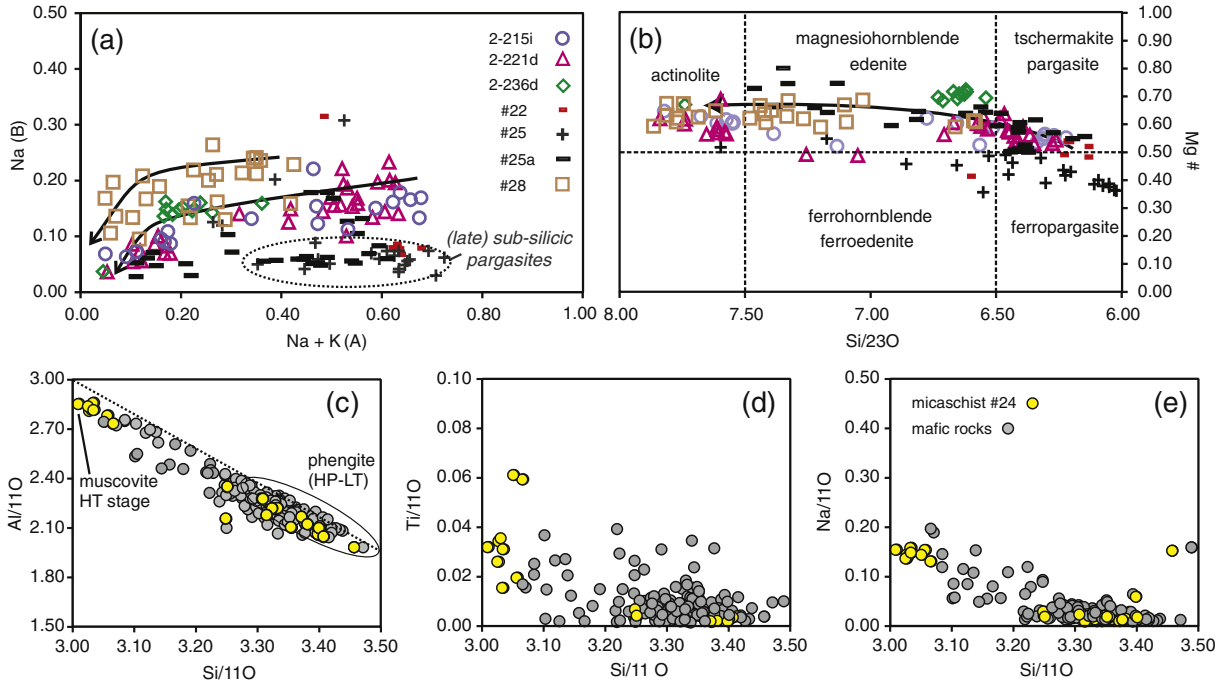

Fig. 5. Electron probe data on amphibole and white mica. a and b. Chemical composition of amphibole according to the classification of Leake et al. (1997). The arrow symbolizes the core-to-rim composition zoning observed in analyzed amphibole. c, d and e. Plot of white mica composition showing the variation of Al, Ti and Na contents as a function of silica content. The dashed line in c indicates the ideal Tschermak substitution.

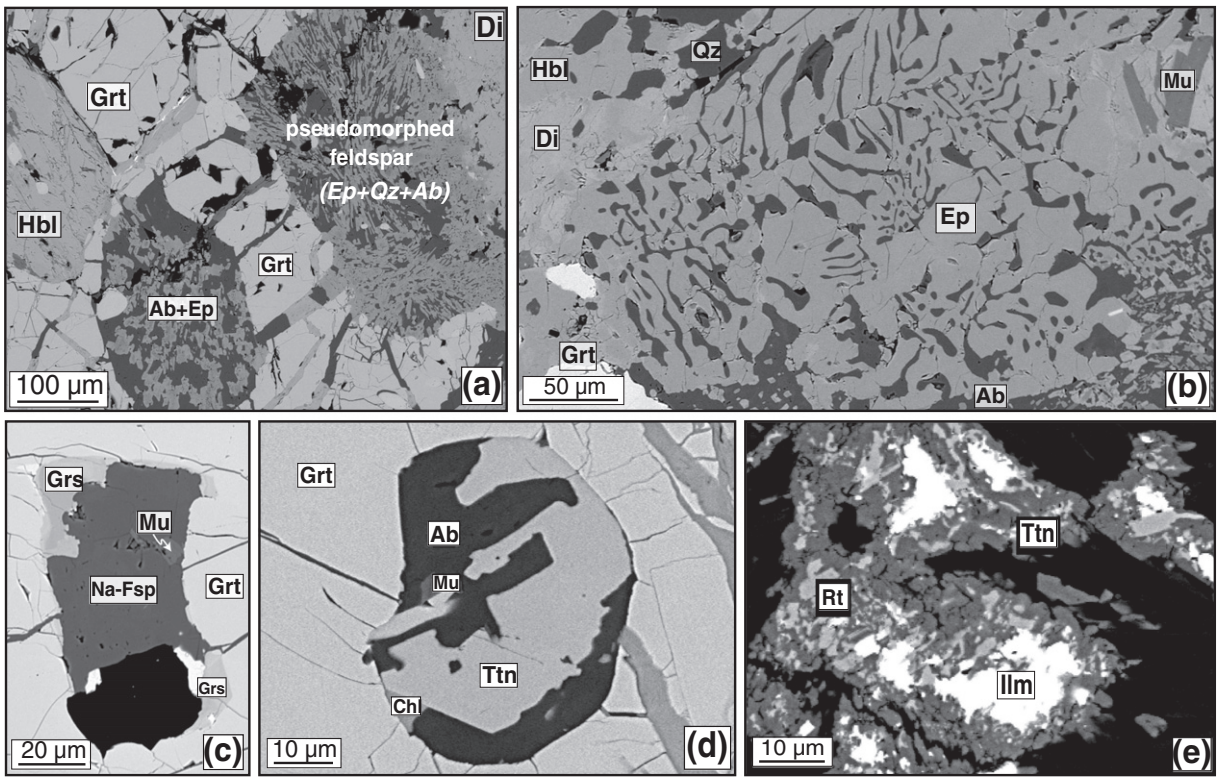

Fig. 6. Back scattered electrons images obtained at the scanning electronic microscope. a. Inclusions of former Ca-Na plagioclase in garnet now fully replaced by a mixture of albite, epidote ± quartz (sample #25). b. View of a myrmekitic ("vermicular") zoisite-rich epidote crystal showing intergrowth features with quartz (dark grey; sample #25a). c. Inclusion of Na-feldspar in a garnet crystal (sample #25a). A discontinuous rim of grossular garnet forms at the contact between the inclusion and the host. d. Rounded, poly-mineralic inclusion included in garnet from sample #25c. e. HT ilmenite is rimmed by rutile, which is overgrown and replaced by titanite during cooling.

of mafic samples as a function of the main metamorphic stages identified here is summarized in Fig. 8. Importantly, orthopyroxene has not been found despite extensive investigation and a systematic check of garnet inclusions.

A texturally late generation of pargasite has been observed in three samples (Electronic Appendix 1, Fig. 5a and b). It comprises post-kinematic crystals with sub-silicic composition, low Na_B (<0.10 apfu) and $Na + K_A$ contents varying from ~0.70 to 0.35, likely recording discrete and later shallow heating (see below).

5.1.2. Trondhjemitic leucosome

Sample #25b (Fig. 3b) corresponds to a fine-grained mixture of 10–20 µm crystals of epidote, albite, muscovite and quartz with locally large porphyblasts of titanite. The presence of diffuse quadrangular shapes in the leucosome suggests the former presence of mm-sized plagioclase crystals now dominantly replaced by epidote and albite. Muscovite crystals are small (<50 µm; 3.05–3.1 Si a.p.f.u.), rare (<2 vol.%) and rimmed by phengite (typically 3.35–3.4 Si a.p.f.u.). Epidote (Ps_{15-20}) often preserves Fe-poorer cores (Ps_{5-10}).

5.1.3. Metasedimentary rocks

Three metasedimentary samples interleaved with mafic lithologies have been studied in detail: a mica schist (#24) and two spessartine quartzites (#22 and #25a; Fig. 3e). The mica schist exhibits abundant muscovite crystals (3.01–3.07 Si a.p.f.u.) rimmed by phengite-rich compositions (3.3–3.47 Si a.p.f.u.; Figs. 5c, d and 9a). These Si-rich rims are in textural equilibrium with chlorite that replaces garnet crystals. In the spessartine quartzite (sample #25a), a former K-feldspar micro-domain is replaced by aggregates of white mica with Ba-rich muscovite cores (up to BaO = 3 wt.%, Si = 3.1 a.p.f.u.) and Ba-depleted phengite rims in textural equilibrium with interstitial albite (Fig. 9b). Garnet crystals from such layers typically range between 10 and 35 mol% spessartine component. In the X-ray maps from Fig. 7a, it is clearly visible that HT Mg-rich garnet I cores are rimmed by 100–200 µm thick Ca-Mn-Fe richer garnet II rims which, in turn, are partly replaced by chlorite. Note that chlorite Mg content spatially varies in Fig. 9a suggesting progressive and partial re-equilibration during cooling. Epidote cores (Ps_{7-12}) exhibit minor zoning with slight increase in ferric iron towards the rims (Ps_{20-22}). When present, amphibole shows a compositional zoning similar to the one described for garnet amphibolites with edenitic-pargasitic cores grading to hornblende rims (Fig. 5). Other accessory minerals are titanite (overgrowing ilmenite/rutile), apatite, pyrite and zircon. Graphite has not been observed.

5.2. Phase relations

The projections presented below have been calculated with software Cspace (Torres-Roldan et al., 2000) and a similar approach to that used by García-Casco et al. (2008) has been applied to the graphical representation of melting phase relations in mafic systems at peak metamorphic conditions. The diagrams are projected from coexisting phases and exchange vectors that allow for complete representation of the compositional space and peak metamorphic mineral compositions. For simplicity, all projections have been made through H_2O, implying $P_{H2O} = P_{total}$, and Fe is treated as FeO_{total}. Note that projection along the plagioclase exchange vector $SiNa(AlCa)_{-1}$ makes albite and anorthite colinear in the ACF diagram, hence preventing discrimination between HT Na-Ca plagioclase and LT albite.

5.2.1. ACF diagram

The near-peak metamorphic event for garnet amphibolite is represented by the assemblage pargasite + epidote ± garnet ± diopside ± Na-Ca plagioclase. Peak topologies are mainly defined by whole rock compositions plotting along the tie-line epidote-amphibole and inside the tie-triangles epidote-pargasite-garnet and epidote-clinopyroxene-garnet (Fig. 10a). The high extent of greenschist facies overprint

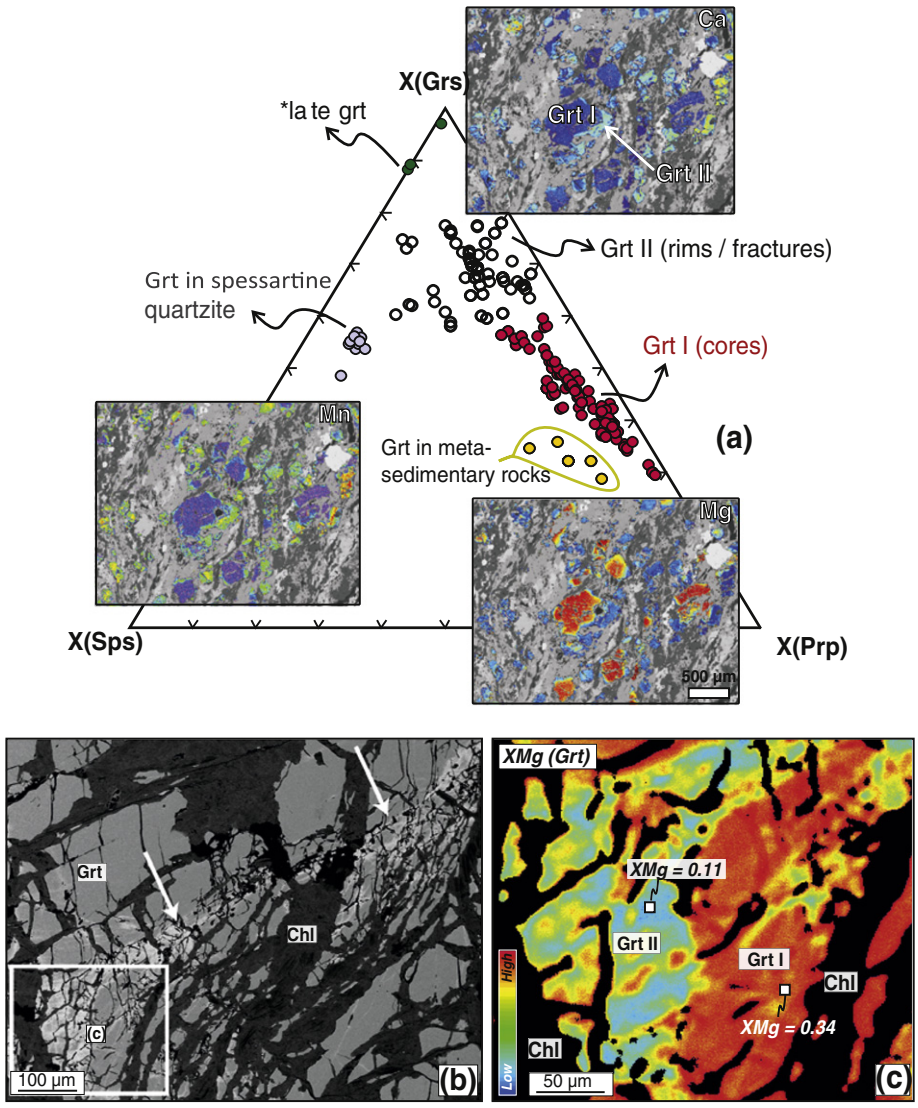

Fig. 7. Garnet chemical zoning and composition. a. Triangular plot showing the composition of Lazaro unit garnet crystals. Garnet from spessartine quartzite plot closer to the Sps corner while Ca-rich garnet observed around the inclusion shown in Fig. 5c corresponds to a grossular composition (green circles). Three X-ray maps (Ca, Mn, Mg) provide a representative view of dismembered HT garnet crystals rimmed by higher Ca-Mn and poorer Mg rims. b. BSE image of a fossilized fracture network (white arrows) cutting through a HT garnet from sample #21. c. X-ray map of the same crystal showing a decrease of the XMg content along the healed fracture network.

prevents concluding whether epidote and/or plagioclase were stable at peak conditions or if the phase relations shown in the ACF diagram represent near-peak conditions slightly after reaching peak temperature. The presence of myrmekite-like intergrowths of epidote and quartz around garnet confirms that epidote has likely been involved in both garnet forming and garnet consuming reactions. As in other instances of (hydrous) melting of mafic rocks, plagioclase may have been totally consumed during melt formation (e.g., García-Casco et al., 2008, and references therein). Samples plot within the tie-triangle plagioclase-amphibole-garnet suggesting that for these bulk compositions plagioclase should have been present during peak conditions. This implies retention of partial melt and crystallization of plagioclase (and epidote minerals) during melt crystallization.

The trondhjemite sample #25b (former melt) plots close to the line separating metaluminous and peraluminous fields of the ACF projection (Fig. 10b), showing that plagioclase, epidote and pargasite can crystallize from this melt composition. Muscovite may also crystallize from this melt, as shown in the ACF diagram of Fig. 10b by the tie-triangle Pl-Ms.-Ep (note that crossing of tie-lines in Fig. 10b represents an artefact of the condensation of the composition space due to projection along the KNa_{-1} exchange vector rather than potential reactions between these phases). The local observation of muscovite inclusions within garnet corroborates this statement.

5.2.2. AFN diagram

For peak conditions the larger part of Lazaro samples plots along the tie-line Prg-Grt and within the tie-triangle Grt-Prg-Di in the AFN diagram projected from (clino)zoisite/epidote (Fig. 10c). This projection also shows that for compositions slightly richer in Na_2O and/or Al_2O_3, plagioclase can coexist in equilibrium with pargasite and garnet (upper right triangle in Fig. 10c). This suggests that samples plotting in the tie-triangle Grt-Prg-Di have experienced a certain amount of melt extraction with respect to potential MORB protoliths, if plagioclase was totally consumed to generate melt. The presence of numerous Na-Ca plagioclase crystals (now pseudomorphed) suggests that plagioclase was in equilibrium with high-T phases shortly before peak conditions. This projection also reveals that for a melt composition plotting within the tie-triangle Grt-Prg-Pl the

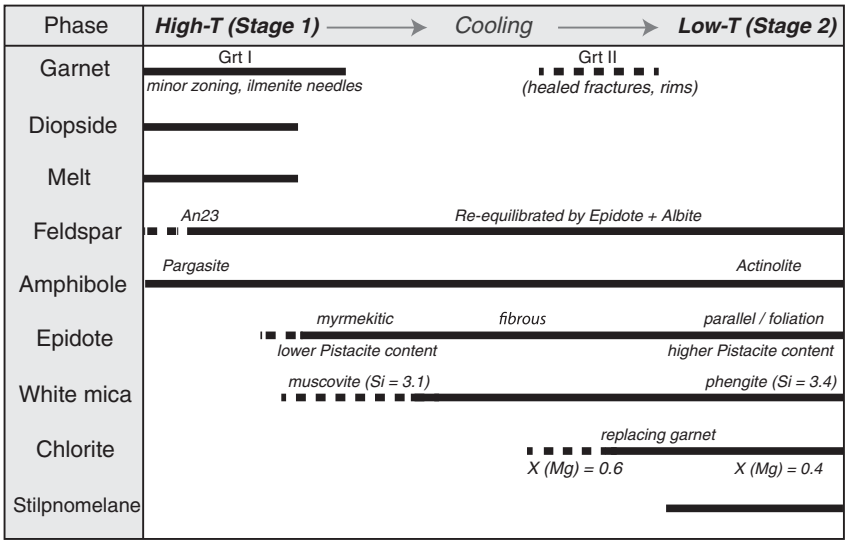

Fig. 8. Occurrence table summarizing the petrological evolution of Lazaro unit samples throughout their metamorphic evolution.

composition of the plagioclase should be around Ab_{80}, similar to the relict inclusions of plagioclase within garnet.

5.2.3. $NaAlO_2 - CaMgO_2 - CaFeO_2$ diagram

In order to track the composition of the plagioclase involved in melt-producing reactions in mafic rocks, an "AFM-like" projection has been used simulating a possible garnet-absent reaction (Fig. 10d). The latter type of reaction provides a unique analytical solution for the composition of plagioclase, provided that melt composition is fixed (trondhjemite #25b) and considering the colinearity of the phases involved (plagioclase, melt and amphibole) (see García-Casco et al., 2008 for details). For a plagioclase composition of Ab_{77}, a degenerate phase relation is defined of the form:

$$Pl + Qtz + Ep + Amp \ (+H_2O) = melt + Ttn.$$

This reaction is characterized by colinearity of plagioclase-pargasite and melt in Fig. 10d, implying a large amount of plagioclase was used to form the melt composition and no formation/consumption of garnet and diopside (i.e., it applies only to garnet/diopside-lacking rocks such as leucosomes; cf. García-Casco et al., 2008). It is worth noting that this degenerate phase relation was likely the exception rather than the rule. There is no reason to claim a prevalence of colinear relations in such a high-variance metamafic chemical system. For Na-richer plagioclase compositions, the phase relationships change from a colinear plagioclase-melt-pargasite topology to the peritectic relation depicted by the reaction:

$$Amp + Pl + Ep + Qtz \ (+H_2O) = melt + Grt,$$

while the garnet consuming reaction:

$$Amp + Pl + Grt + Qtz \ (+H_2O) = melt + Ep$$

occurs for Ca-richer plagioclase (cf García-Casco et al., 2008). In the case of the Lazaro unit, the peritectic garnet-forming reaction took place, as indicated by the formation of porphyroblastic and megablastic garnet in melanosomes.

The approach presented above graphically confirms the involvement of sodic plagioclase (Ab_{77}) in the peritectic garnet-forming reactions. This inference can be extended to the case of diopside-bearing assemblages and for the general case of either H_2O-saturared or H_2O-subsaturated systems (e.g., Green, 1982; García-Casco et al., 2008).

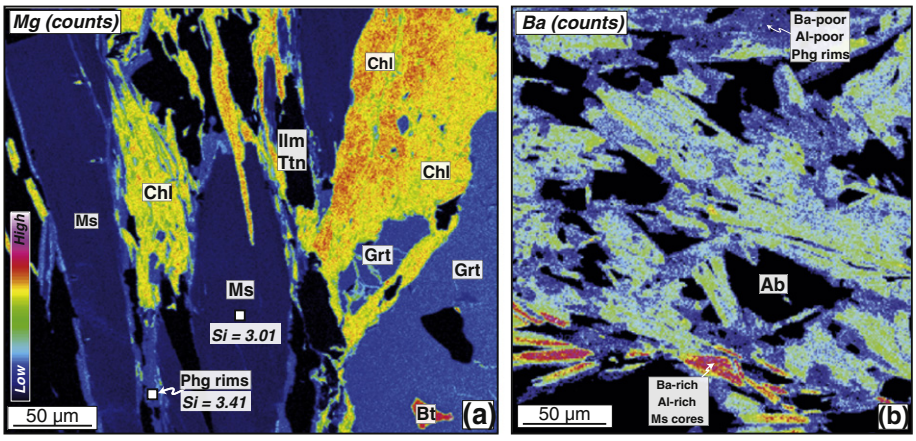

Fig. 9. X-ray maps of metasedimentary rocks from the Lazaro unit. a. Mg content map showing the effect of Tschermak substitution visible as high Mg, Fe and Si contents in the rims that form around muscovite rims (sample #24). Note the heterogeneous zoning pattern of chlorite, partly replacing garnet. b. X-ray map showing the barium content of a pseudomorph after K-feldspar in sample #25a. Barium-rich zones match with Al-richer muscovite cores while Ba-depleted crystals exhibit lower aluminum contents.

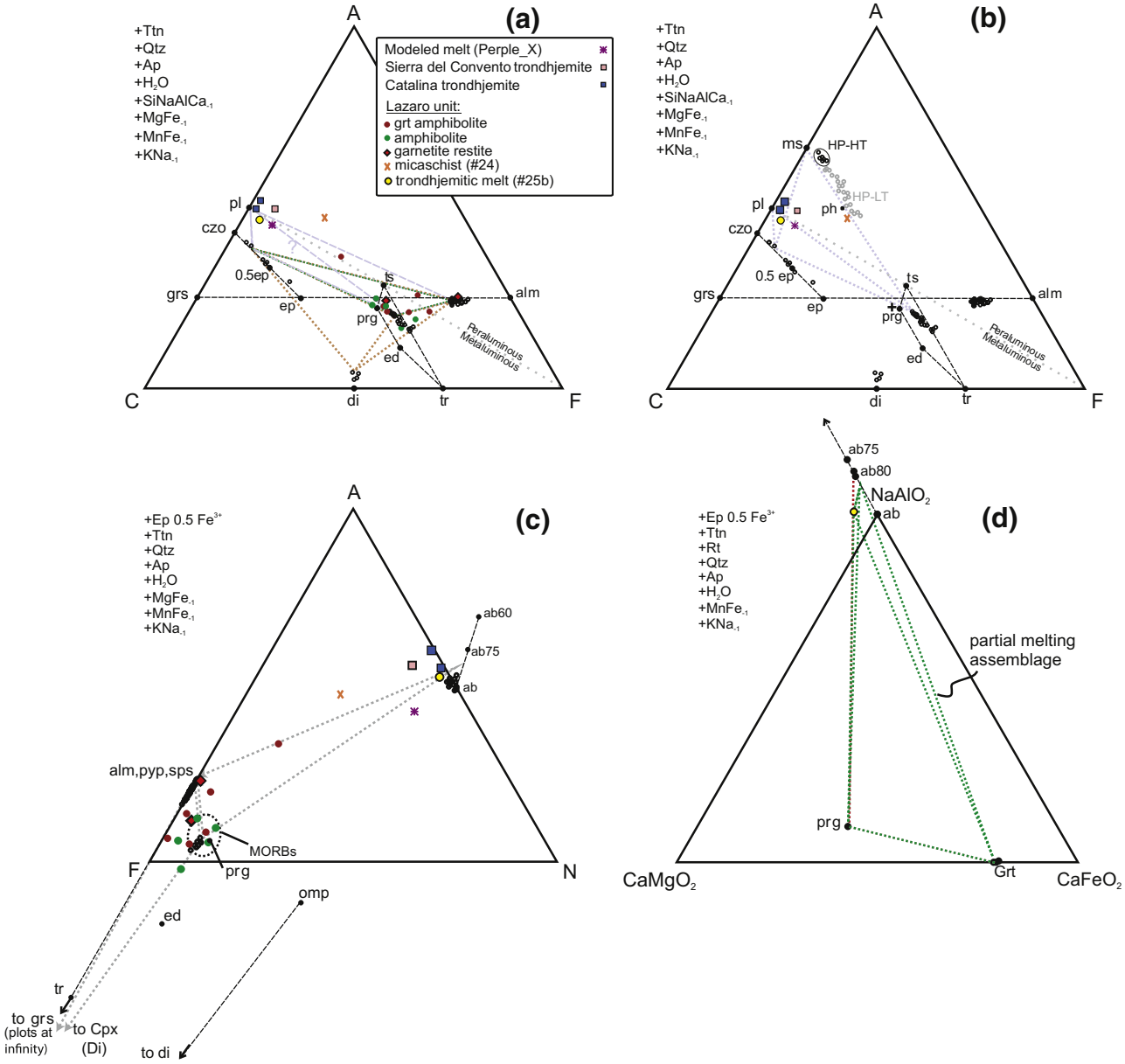

Fig. 10. ACF, AFN diagrams (a–c) and AFM-like diagram (d) showing peak near-metamorphic and melt-related assemblages of representative samples of mafic rocks from Lazaro unit. Some mineral end-members and analyzed mineral compositions are plotted. Also bulk trondhjemite compositions from Sierra del Convento (Cuba; García-Casco et al., 2008) and from the Catalina Island (samples 3755 and 3754 from Sorensen, 1988) are plotted for comparison. a. ACF diagram of garnet amphibolite and amphibolite. Dashed green lines: tielines connecting epidote, garnet and pargasite. Dashed brown lines: tielines connecting epidote, diopside, pargasite and garnet. Dashed purple lines: tielines connecting plagioclase, epidote, pargasite and garnet (see text for explanation). b. ACF diagram representing magmatic minerals that can crystallize from the melt. The black cross represents the MORB composition. c. AFN diagram of garnet amphibolite and amphibolite. Dashed grey lines connecting diopside, garnet and pargasite (left lower triangle), and garnet, pargasite and plagioclase (An_{80}) (right upper triangle). The area defined by the black dashed line comprises the MORBs position in the projection. See text for explanation. d. AFM-like diagram representing partial melting assemblages. The red dashed line represents the degenerated phase relationships defined by the alignment of pargasite, melt and plagioclase (An_{77}). The green dashed line connects pargasite, melt, garnet and plagioclase (Ab_{85}) representing a peritectic reaction with melt and garnet as products. See text for explanation.

5.3. Bulk rock geochemistry

5.3.1. Mafic rocks

Garnet amphibolite and amphibolite show basic compositions with SiO_2 varying between 41 and 52 wt.%, corresponding to tholeiitic basalt and picro-basalt ($Na_2O + K_2O = 0.34$ to 4.26, Table 2). One mafic orthogneiss is richer in SiO_2 (55.54 wt.%) and plots in the basaltic andesite field due to the presence of a thin metachert band (which does not impact the trace element pattern typical of a MORB). To constrain the tectonic setting in which the protoliths of garnet amphibolite and amphibolite formed, the pattern of trace elements with relatively immobile behavior during (low temperature) seafloor alteration and high temperature metamorphic conditions have been considered (mainly HREE and some HFSE).

Garnet amphibolite and amphibolite have a nearly flat chondrite-normalized REE pattern and are distributed between average N-MORB and E-MORB compositions (Fig. 11a and b). Their composition overlaps with blueschists and garnet amphibolites from the underlying HP-LT Almagro Complex (Fig. 11a). Samples with anomalous patterns have been plotted separately (Fig. 11b). These patterns suggest modifications due to (i) melt extraction/garnet fractionation in garnet-bearing rocks (relatively higher HREE concentrations with respect to enriched MORBs and negative Eu anomaly); (ii) late hydrothermal/metasomatic processes (positive Eu anomalies and fractionated pattern characterized

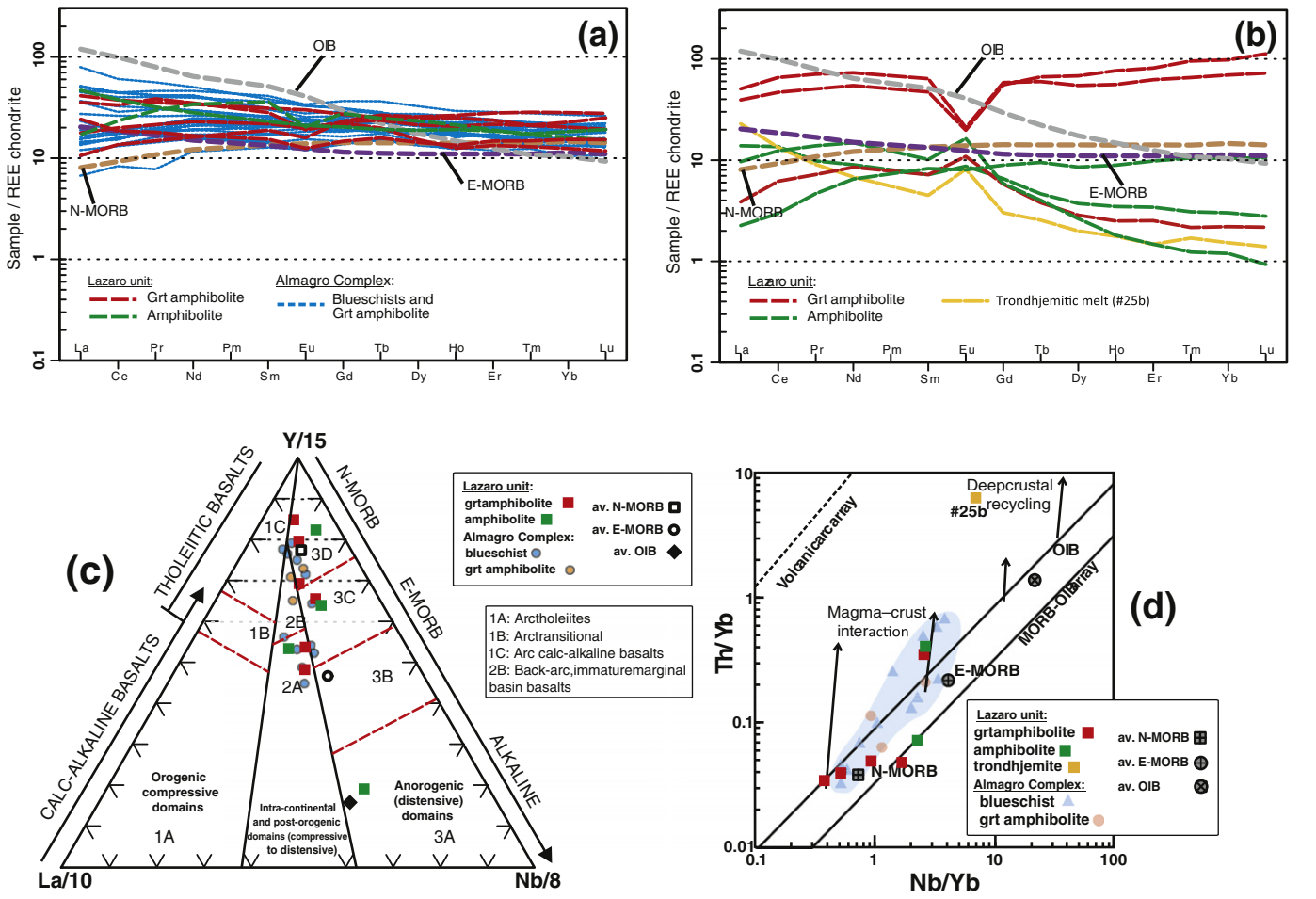

Fig. 11. Geochemical data on Lazaro unit rocks. a. REE plot of garnet amphibolite and amphibolite from the Lazaro unit. This data is compared with underlying metabasalt from the Almagro Complex (Hyppolito et al., 2016). OIB, N-MORB and E-MORB compositions from Sun and McDonough (1989). b. REE plot for more samples from the Lazaro unit departing from the global trend. Those anomalous compositions may be related to melt extraction and/or garnet crystallization processes. c–d. Y-La-Nb diagram of Cabanis and Lecolle (1989) and Th/Yb versus Nb/Yb diagram of Pearce (2008), respectively, showing the oceanic affinity of Lazaro rocks.

by lower HREE contents in "pegmatite-like" samples); (iii) retrogression-related contamination characterized by slightly higher LREE concentrations in garnet amphibolites with evidence of melt loss (e.g., samples of case (i)).

The Y-La-Nb diagram (Cabanis and Lecolle, 1989) is useful for discriminating basalts formed in convergent and extensional settings. Fig. 11c reveals the non-orogenic affinity of the Lazaro unit rocks, which mainly plot in the field of extension-related oceanic basalts, and are distributed along the N-MORB-E-MORB-OIB trend. Three samples plot within the field of possibly contaminated undifferentiated basaltic magmas or continental basalts, likely reflecting local La enrichments. The Th/Yb versus Nb/Yb diagram of Pearce (2008) (Fig. 11d) is suited to track mantle sources (Nb/Yb) and the effects of crustal components (Th/Yb), making use of two highly and nearly equally incompatible elements in basaltic magmas (Th and Nb). However, these two elements have different behaviors during subduction, being non-conservative and conservative, respectively, hence defining a sensitive indicator of crustal involvement due to magma–crust interaction or to inheritance of subduction components (Pearce, 2008). In the Th/Yb vs Nb/Yb diagram (Fig. 11d) Lazaro rocks are distributed between N-MORB and E-MORB, confirming their oceanic affinity (with minor crustal contamination for some samples).

5.3.2. Trondhjemitic leucosome

Sample #25b belongs to the trachyte field in the TAS classification (total alkalis-silica), with 61 wt.% SiO_2, high Na_2O (8.02 wt.%) and very low K_2O (0.68 wt.%) contents, low contents of FeO_t and MgO (1.27 wt.%, 0.59 wt.%, respectively), and high mg# (0.45, Table 2). This sample is classified as trondhjemite, following the molecular normative (CIPW) Ab-An-Or diagram of O'Connor (1965) and the fields of Barker (1979) (not shown), and it is slightly peraluminous with an Alumina Saturation Index (ASI) of 1.17, plotting at the transition between metaluminous ($0 \le ASI \le 1$) and peraluminous fields ($1 \le ASI \le 3$) (not shown). The chondrite-normalized REE pattern shows enrichment in light REE (LREE) revealing a fractionated pattern (Fig. 11b). The positive Eu anomaly corroborates the presence of plagioclase in melt forming reactions. It is also in agreement with negative Eu anomalies in garnet bearing samples with evidences of melt loss.

6. Thermobarometry

6.1. Single-equilibrium thermobarometry

In order to constrain the temperature reached by the Lazaro unit rocks during the HT metamorphic event, the garnet-clinopyroxene thermometers of Ravna (2000) and Ellis and Green (1979) have been used for samples #25 and #2-31b, in which peak metamorphic diopside has been preserved during retrogression. These temperatures have been calculated for a fixed pressure of 1.2 GPa. This pressure estimate was obtained on a garnet amphibolite sample (#27) following the calibration of Kohn and Spear (1990) for Grt-Amp-Pl-Qz assemblages. Averaged results are given in Table 3. Temperature estimates based on

Table 3
Thermobarometric results on Lazaro unit garnet amphibolites and granulite-facies rocks using the calibrations of [1] Kohn and Spear (1990), [2] Ravna (2000) and [3] Ellis and Green (1979). Average P calculations have been made following Powell and Holland (1994).

Sample	Method	Average mineral composition	Fixed parameter	Results (min–max)
#27	Grt-Amp-Pl-Qz barometer [1]	$Alm_{58}Prp_{20}Grs_{22}/An_{23}$/Amph: Si = 6.18, Na(A) = 0.32	T = 750 °C	P = 1.11–1.32 GPa
#25	Grt-Cpx thermometer [2]	$Alm_{56}Prp_{8}Grs_{32}Sps_{4}/Di_{55}Ca\text{-}Ts_{9}Hed_{34}Jd_{3}$	P = 1.2 GPa	T = 707–741 °C
#25	Grt-Cpx thermometer [3]	$Alm_{56}Prp_{8}Grs_{32}Sps_{4}/Di_{55}Ca\text{-}Ts_{9}Hed_{34}Jd_{3}$	P = 1.2 GPa	T = 769–792 °C
#2-31b	Grt-Cpx thermometer [2]	$Alm_{59}Prp_{14}Grs_{26}Sps_{1}/Di_{56}Ca\text{-}Ts_{5}Hed_{33}Jd_{6}$	P = 1.2 GPa	T = 682–692 °C
#2-31b	Grt-Cpx thermometer [3]	$Alm_{59}Prp_{14}Grs_{26}Sps_{1}/Di_{56}Ca\text{-}Ts_{5}Hed_{33}Jd_{6}$	P = 1.2 GPa	T = 754–763 °C

Ravna (2000) yield c. 50 °C cooler temperatures than those based on Ellis and Green (1979). These results suggest that the Lazaro unit reached peak temperatures in the range 700–780 °C.

6.2. Chlorite-phengite thermobarometry

In order to estimate the P-T conditions for the retrogression of Lazaro unit rocks, we used for sample #29a an approach similar to the one initially developed by Berman (1991) (see detailed results and approach in Electronic Appendix 2). The MATLAB software "Kit Chl-Phg" has been used here to perform these calculations (method and thermodynamic database used is described in Vidal et al., 2001, Dubacq et al., 2010 and Angiboust et al., 2014). This software enables a statistical exploration of chlorite-phengite pairs and the identification of equilibria between end-members. The multivariant reactions are manually plotted and P-T conditions for curve intersection are derived. For sample #29a, 28 equilibria satisfying validity criteria have been found. The average of these estimates yields a temperature of 541 ± 59 °C and a pressure of 1.12 ± 0.19 GPa. Despite a relatively large spread, these results indicate that the retrograde path (Stage 2) proceeded under relatively high pressures, similar to stage 1 pressure conditions.

6.3. Pseudosection modeling

The P-T location of the peak metamorphic assemblage and the nature of melt-producing reactions have been investigated using the pseudosection modeling approach and the software package Perplex (v.6.7.2; Connolly, 2005). Evaluating the effective bulk rock composition is difficult because these rocks have been subject to variable degrees of melt extraction/infiltration. Therefore, none of the bulk rock compositions given here can be used to model phase relationships at pre-peak conditions. Trace-element composition and phase relationships (Fig. 11) have shown that most Lazaro rocks originally derive from a protolith close to a MORB composition. Hence, we decided to use an average of c. 5000 glass analyses compiled from the PetDB database (http://www.earthchem.org/petdb; composition given in Fig. 11). The thermodynamic modeling has been performed in the NCKFMASH system (manganese and ferric iron have been neglected for simplicity). Activity models used here are the following: garnet and biotite (White et al., 2007), clinopyroxene (Holland and Powell, 1996), orthopyroxene (Powell and Holland, 1999), amphibole (Dale et al., 2005), chlorite (Holland et al., 1998), white mica (Smye et al., 2010), melt (White et al., 2001 and White et al., 2007), and feldspar (Fuhrman and Lindsley, 1988).

The amount of H_2O in the system is a critical parameter as it influences the position of the solidus as well as the amount of melt produced (e.g. Vielzeuf and Schmidt, 2001). We first ran a T-[$H_2$0] pseudosection for a fixed pressure of 1.2 GPa in order to assess the optimal amount of water needed to accurately reproduce petrogenetic observations (Fig. 12a). This diagram shows that the observed peak paragenesis of hornblende-garnet-diopside-feldspar ± quartz is achieved for a T range between 670 and 780 °C and initial water amounts between 1.5 and 3.5 wt.%. Fig. 12b shows modal amounts of peak metamorphism mineral phases as a function of initial water content. Our results indicate that increasing the amount of H_2O in the system leads to a decrease of feldspar modal amount (Fig. 12b; see also Green, 1982). Given the apparent scarcity of feldspar within amphibolite to HP-granulite-facies assemblages (between 5 and 15 vol.%; e.g. Fig. 3a), we believe that an amount of 3 wt.% H_2O is a reasonable estimate for calculating a P-T grid for this bulk composition. The result of this calculation for a fixed amount of 3% H_2O is shown in Fig. 12c. The P-T field obtained for peak metamorphic conditions is in agreement with peak P-T estimates yielded by conventional thermobarometric methods (see Section 6.1). These calculations imply that a fluid infiltrated the Lazaro unit during peak metamorphism and this triggered partial melting ciose to the solidus. At this stage under fluid flux, hornblende is stabie at near 750 °C, but was partially consumed to form diopside, garnet and melt (Fig. 12d). This statement is in agreement with petrological observations demonstrating the amphibole has not been completely consumed at the time of partial melting at peak T (e.g. Fig. 3f). The calculated Na_B content of peak amphibole at 750 °C and 1.2 GPa is 0.25 a.p.f.u., in agreement with EMP data (Table 1; Fig. 5). The calculations presented here show that both amphibole and epidote were the hydrous phases involved in melting reactions, in agreement with natural and experimental observations at pressures higher than 1.0 GPa (e.g. Vielzeuf and Schmidt, 2001; García-Casco et al., 2008). On the other hand, the presence of hornblende and feldspar in the peak metamorphic assemblage indicates that temperature never exceeded ca. 790 °C (Fig. 12c and d).

6.4. Average P-T

Additional P-T calculations have been carried out using the multi-equilibrium thermobarometric approach. Optimal thermobarometry (Powell and Holland, 1994) was performed using the software THERMOCALC (Holland and Powell, 1998, version 3.33). End member activities and their uncertainties were calculated with the software AX (Holland, unpublished). Calculations were performed with a pure H_2O-fluid.

Due to large error bars obtained with average P-T calculations, we fixed the temperature to evaluate pressure during peak T metamorphism. We calculated the average-P for a temperature series between 650 °C and 850 °C with 25 °C steps on sample #25 (epidote-clinopyroxene-hornblende-garnet-quartz), which resulted in a pressure of 1.37 GPa (sd = 0.314 GPa, fit = $0.71 < 1.61_{sigfit}$). This P estimate yields a P range in agreement with the results from the other methods presented above.

7. Geochronology

7.1. Rb-Sr geochronology

The Rb-Sr internal mineral isochron approach is particularly well suited for dating ductile deformation events in white-mica bearing metamorphic rocks. Deformation-induced recrystallization and re-equilibration of mineral phases (such as white mica, albite, apatite and titanite) leads to complete Sr-isotopic re-equilibration and reset of ages under moderate and high temperature (Inger and Cliff, 1994). Isotopic inheritance due to incomplete resetting of the pre-deformation isotopic system may lead to isochron patterns showing partial disequilibrium (e.g. Angiboust et al., 2014). We analyzed different grain-size fractions in order to (i) better evaluate the importance of incomplete resetting of white mica isotopic composition and (ii) detect potentially

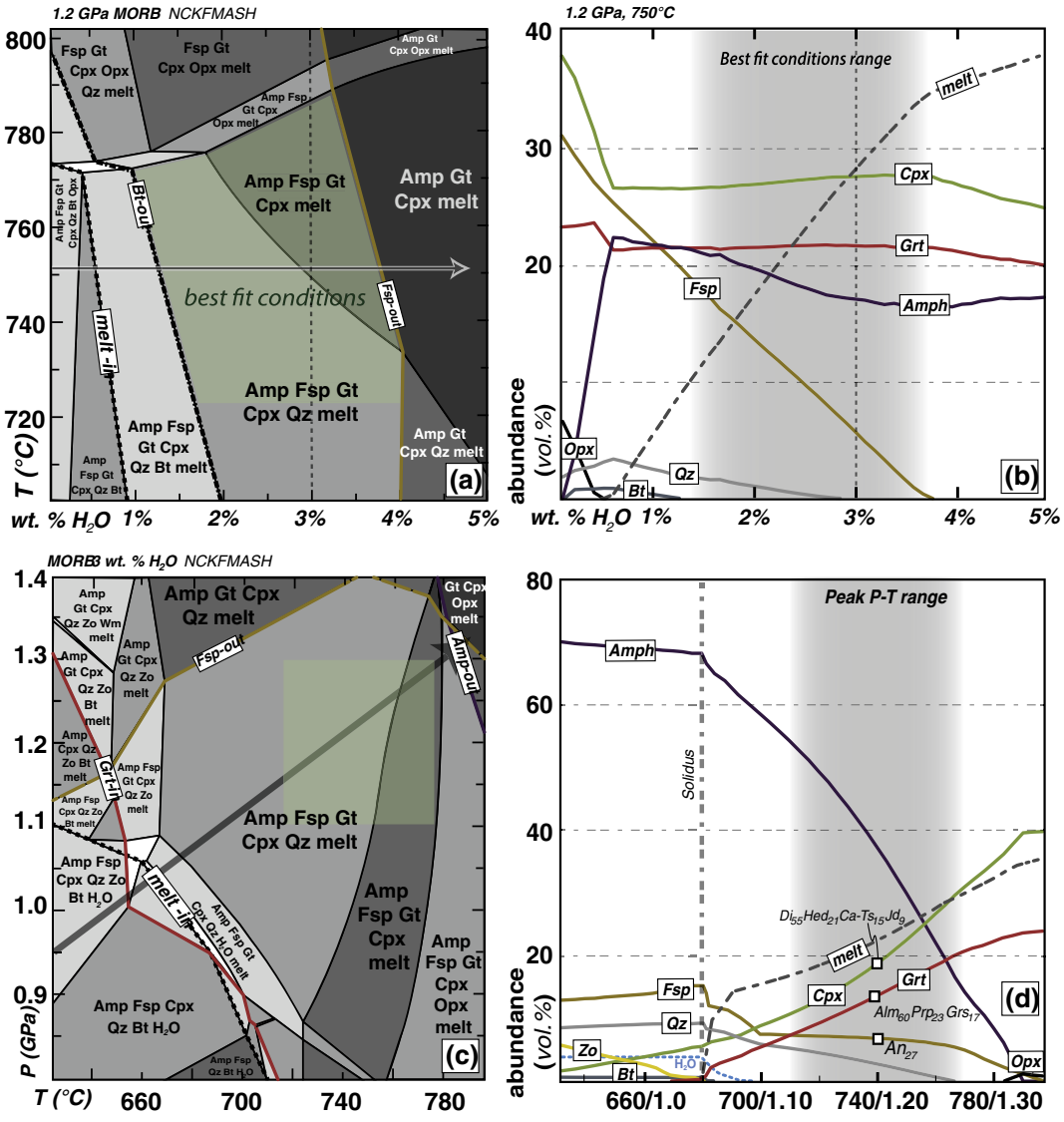

Fig. 12. Pseudosection modeling results performed on a MORB composition in the NCKFMASH system using the software Perplex. a. T-[H_2O] pseudosection calculated at 1.2 GPa for a MORB composition showing theoretical phase assemblages in the best-fit region (determined using conventional thermobarometry; see text). The HT-limit of the best-fit region is based on Fsp disappearance. The bulk composition (in wt.%) used for the modeling is the following: SiO_2(50.9)Al_2O_3(14.5)FeO(10.8)MgO(8)CaO(10.95)Na_2O(2.78)K_2O(0.16). b. Modal evolution of mineral abundances near peak conditions calculated along the path depicted in figure a (grey arrow). The observation of coeval garnet, diopside, amphibole, melt and feldspar (<10 vol.%) in best-preserved samples (e.g. #25) suggests that around 3 wt.% of water was present during melting in the best-fit P-T window. c. P-T pseudosection calculated using 3 wt.% free H_2O and the same MORB composition. The transparent box corresponds to the best-fit range based on conventional thermo-barometric approach (see text). The grey arrow corresponds to the hypothetical prograde P-T gradient assumed for Lazaro unit HP rocks. Given the mobility of the fluid phase and the opening of the system, we emphasize that this diagram is only shown as an indication since the location of the fields depends on the amount of fluid in the system which can substantially vary a function of fluid influx and melt extraction. Note that the unexpected presence of melt in the upper left corner of the pseudosection may arise from the use of a haplogranitic melt model for this mafic bulk composition. d. Modal evolution of mineral abundances near peak conditions calculated along the prograde path localized in figure c. The best-fit P-T range corresponds to the box shown in figure c. Calculated mineral compositions are shown for comparison to mineral EPM analyses.

protracted recrystallization or deformation histories of the studied rocks. This approach generally yields younger apparent ages for smaller grain-size white mica fractions (Angiboust et al., 2014). Thus, younger apparent ages calculated using small grain-size mica fraction can be considered as maximum age estimates for the end of ductile deformation. For Rb-Sr dating of the tectonic overprint we selected samples with pervasive, fine-grained mylonitic foliation and devoid of porphyroclasts in order to avoid isotopic relics.

Three metasedimentary samples from the Lazaro unit showing white-mica bearing mylonitic deformation were processed for multi-mineral Rb-Sr geochronology in order to constrain the timing of the LT tectonic overprint reported here (stage 2; complete dataset available in Electronic Appendix 3). The three datasets obtained here show variable degrees of isotopic disequilibrium confirming microtextural evidence that indicates multi-stage deformation events (see Section 6; Fig. 13). Sample #24 (metasedimentary rock), showing large muscovite crystals rimmed by phengite, exhibits disequilibrium textures and ages (as expected from micro-chemical mica zoning imaging; Figs. 9a and 13a). An age calculation attempt using the smallest analyzed muscovite fraction (160-125 μm) and apatite leads to a maximum age for the end of deformation at 116.3 ± 1.8 Ma. Similar disequilibrium has been obtained for sample #23-b3 (Fig. 13c). The age of 83.1 ± 1.4 Ma, calculated using the smallest analyzed phengite fraction and albite-quartz aggregates, is considered to be a reliable estimate for the maximum age for the end of LT deformation. An age of 94.6 ± 7.2 Ma has been calculated for sample #29a, a LT-mylonite located on the contact between the Lazaro unit and the Almagro blueschist complex (Puerto shear zone; Fig. 1c). The 116.3 Ma age for sample #24 was obtained from muscovite

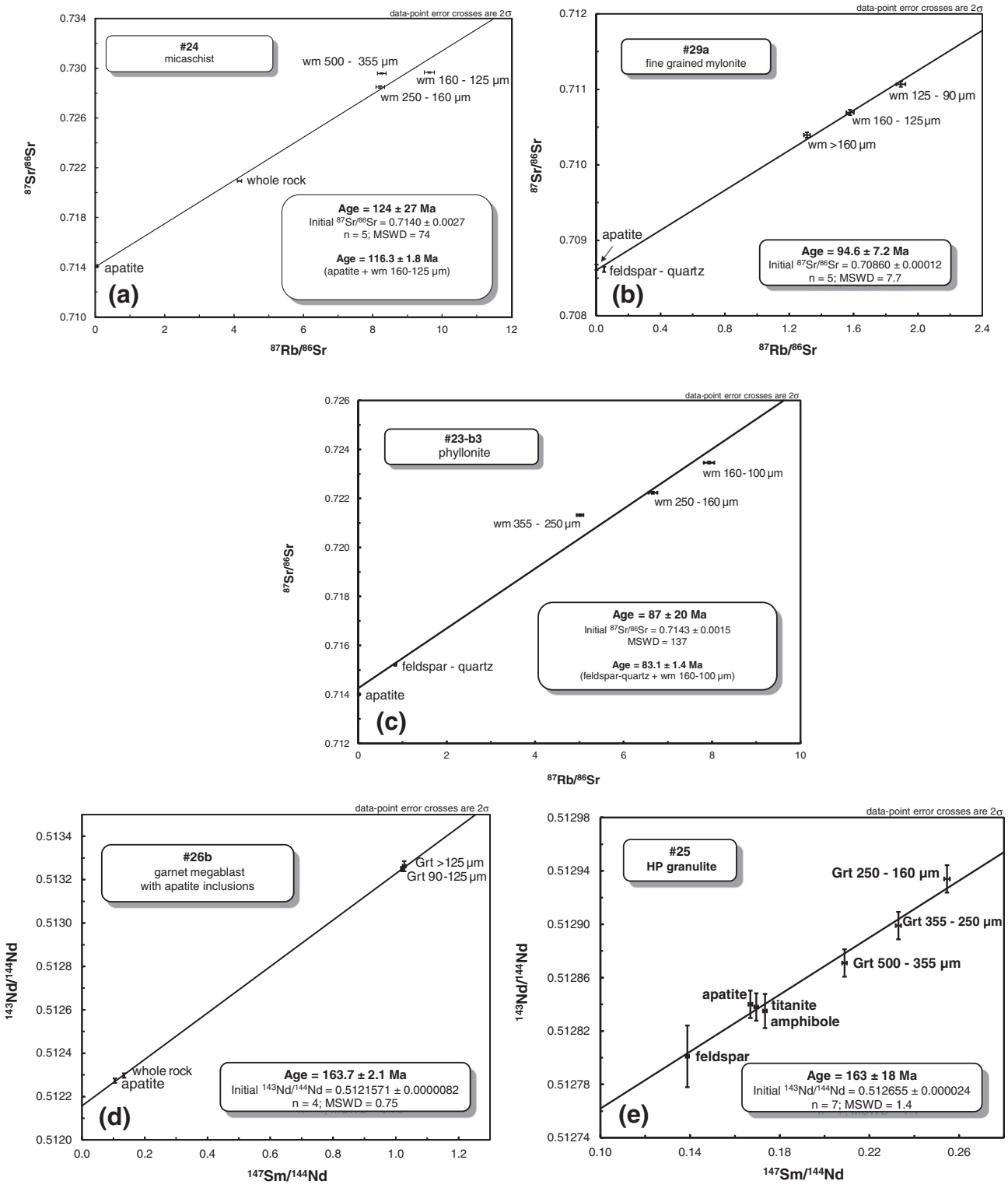

Fig. 13. Geochronological results using Rb-Sr (a, b, c) and Sm-Nd (d, e) techniques.

that formed by replacement of stage 1 K-feldspar during cooling (Fig. 9a). This age is clearly older than the two other younger ages of 82–85 Ma and 87–101 Ma (respectively samples #23b3 and #29a), calculated using phengite crystals from the mylonitic foliation (and not muscovite as for #24). This distribution therefore shows that Lazaro unit rocks underwent at least two stages of tectonic overprint between c. 120 Ma and c. 80 Ma leading to incomplete re-equilibration that yields the large age spread for end-of-deformation estimates.

7.2. Sm-Nd geochronology

In order to constrain the age of peak T metamorphism, we processed two samples: a garnet megablast-bearing sample (#26b; Fig. 3d) and a garnet-bearing melanosome (sample #25; Fig. 3a). Petrological investigations have shown that these garnet crystals are only made of Grt 1 generation and are only barely zoned. The isochron shown in Fig. 13d, calculated combining two fractions of garnet fragments, the whole

rock and the apatite crystals (see Fig. 4d) yielded a precise isochron age of 163.7 ± 2.1 Ma. This age is consistent with 163 ± 18 Ma derived for granulite-facies sample #25 using different garnet fractions, titanite, apatite, hornblende and feldspar (Fig. 13e). The large uncertainty associated with this age is due to the low spread between $^{147}Sm/^{144}Nd$ ratios in the analyzed mineral fractions (see complete dataset in Electronic Appendix 3).

7.3. Zircon U-Pb geochronology

SHRIMP U-Th-Pb results are presented in Fig. 14 and the complete analytical dataset given in Electronic Appendix 4. Metasedimentary sample #24 contains zircon with a wide range of sizes and morphologies, as expected for metasedimentary zircon. In this sample we measured 71 spots, 62 of which yielded concordant ages (discordance ≤ ±5%). The ages obtained may be divided into three groups.

The first group consists of Precambrian zircons with colorless rounded cores and rare rims, with a size of up to 125 μm × 50 μm. Under the electron microscope most grains show bright cathodoluminescence (CL) signals and oscillatory zoning (Fig. 14a). Eight U-Th-Pb measurements on 6 zircon grains yielded concentrations of U in the range 71–827 μg/g and Th in the range 14–177 μg/g with Th/U ≈ 0.02–0.75 (Fig. 14d). They do not contain common lead (f206 ≈ −0.01 to 0.38%) and are concordant (discordance ≈ −3.4 to 2.4%). The $^{206}Pb/^{238}U$ age comprises two Mesoproterozoic, 1277–1062 Ma, one Neoproterozoic (Tonian), 723 ± 40 Ma, one Neoproterozoic (Cryogenian), 678 ± 30 Ma, and four Neoproterozoic (Ediacaran), 629–552 Ma, zircons (Electronic Appendix 4 and Fig. 14b).

The second group is of Paleozoic-Triassic age and is made of stubby medium-sized cores, 75 μm × 50 μm, with oscillatory zoning, irregular terminations and bright CL signals (Fig. 14a). Twenty-five U-Th-Pb measurements on 25 zircon grains yielded high concentrations of U (124–1132 μg/g) and Th (15–630 μg/g) with Th/U ≈ 0.02–1.8 (Fig. 14d). They contain small amounts of common lead (f206 ≈ −0.22 to 0.54%) and all are concordant (discordance ≈ −0.8 to 3.4%). The $^{206}Pb/^{238}U$ age comprises two Cambrian, 524–495 Ma, three Ordovician, 472–455 Ma, one Silurian, 431 ± 6 Ma, three Devonian, 414–360 Ma, two Carboniferous, 350 ± 5 Ma and 320 ± 5 Ma, and fourteen Permian, 298–266 Ma, zircons (Electronic Appendix 4 and Fig. 14b). This 298–266 Ma core age group represents a prevalent age signal in the

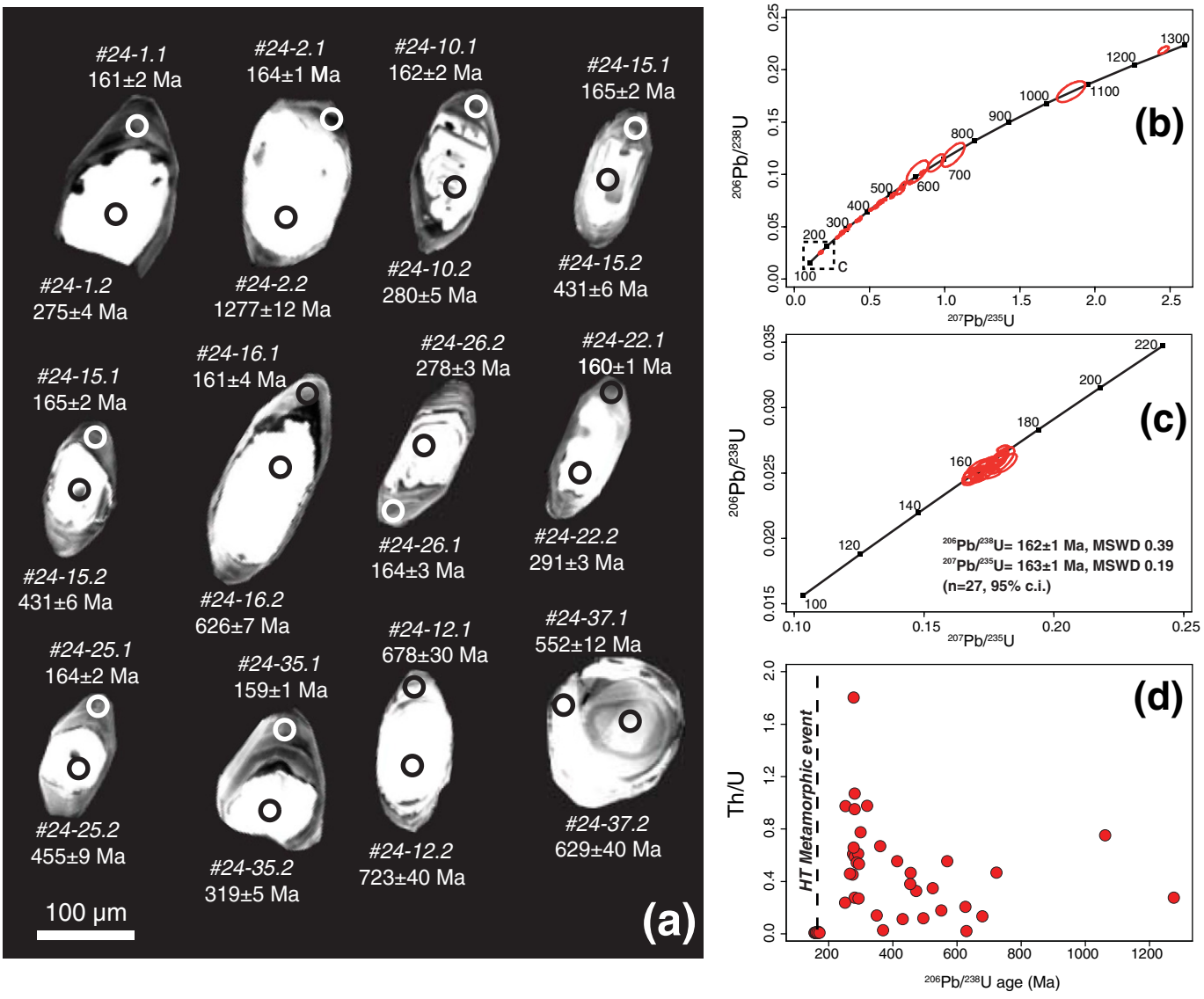

Fig. 14. Results from the U-Th-Pb zircon dating. a. Cathodoluminescence images and $^{206}Pb/^{238}U$ ages of representative analyzed zircon grains from the metasedimentary rock #24. Note that all low cathodoluminescence overgrowths on older grains yield an age c. 162 Ma. Note also the evidence for dissolution of numerous zircon cores during the stage 1 HT event. b. Wetherill concordia plot for sample #24. c. Wetherill Concordia detail for low CL signal rims. d. Zircon Th/U ratio vs $^{206}Pb/^{238}U$ ages, note the lowest Th/U values of low CL signal, c 162 Ma, rims.

sedimentary zircon record. Two zircon grains show highly luminescent cores, 100 μm × 50 μm, with Triassic $^{206}Pb/^{238}U$ ages of 251–250 Ma (Fig. 14a).

The third group is Middle-Late Jurassic (Callovian-Oxfordian) and comprises small (60 μm × 30 μm), dark cathodoluminescence rims overgrowing all zircons in the sample, independent of their age (Fig. 14a). Some of these rims also show oscillatory zoning (Fig. 14a). Twenty-seven of these rims contain high concentrations of U (751–1604 μg/g) and low Th (6–15 μg/g), with the lowest Th/U ≈ 0.006–0.01, combined with only small proportions of common lead (f206 < 0.34%). All of them are concordant (discordance ≈ −1.4 to 3.2%). The weighted mean (errors reported at 2σ) of the uncorrected $^{206}Pb/^{238}U$ ages, 162 ± 1 Ma (MSWD = 0.39), is virtually identical to the $^{207}Pb/^{235}U$ age of 163 ± 1 Ma (MSWD = 0.19; Electronic Appendix 4 and Fig. 14c).

8. Discussion

8.1. Pressure-Temperature-time history of Lazaro unit

Lazaro unit rocks reveal a two-fold tectono-metamorphic history visible in the structural record in the field and in the mineral zoning patterns. The prograde, burial history has not been preserved due to the high temperature of peak metamorphism and a long-term re-equilibration during cooling and exhumation (see also Willner et al., 2004b). Our P-T estimates show that peak metamorphic conditions reached c. 1.2 GPa and 750 °C (~40 km depth using an integrated rock density of 3) at the transition from the albite amphibolite facies to the HP granulite fields (O'brien and Rötzler, 2003). This metamorphic event led to the formation of variable amounts of melt due to hydrous fluid influx and to the crystallization of a large amount of peritectic garnet associated with garnet-bearing melanosomes. Some of these HT garnet crystals preserve oriented ilmenite and rutile exsolution needles, which are typical features of HT/HP and UHT terranes worldwide (Fig. 4c; e.g. Snoeyenbos et al., 1995; Ague and Eckert, 2012). Rounded, polymineralic inclusions in garnet also recall the texture of melt inclusions ("nanogranites") increasingly reported in migmatitic and granulitic terranes worldwide (Fig. 4g; Cesare et al., 2009). Some samples (e.g. #25a; Fig. 6b) exhibit myrmekite-like intergrowths of epidote and quartz spatially associated with peritectic garnet in melanosomes. Such texture has been observed in magmatic, migmatitic and pegmatitic rocks and interpreted to have formed by the crystallization of phases from a silicate melt at pressures exceeding 0.8 GPa in the presence of a hydrous fluid (Zen and Hammarstrom, 1984 and references therein; Jones and Escher, 2002). The absence of this magmatic epidote in some samples may be related to local H_2O-undersaturation during the stage 1 event or, more likely, to insufficient pressure. The latter could indicate that these rocks stayed just in the limit of the "epidote-in" reactions, at c. 1.2 to 1.3 GPa (e.g. García-Casco, 2007), which may have precluded the formation of epidote from some bulk compositions.

The SHRIMP U-Th-Pb zircon rims from the metasedimentary rock sample #24 yield near-peak metamorphic ages of c.161–164 Ma around detrital grains, in good agreement with multimineral Sm-Nd ages of samples containing peritectic garnet (163 ± 2 Ma and 163 ± 18 Ma; Figs. 13d, e and 14). Altogether our results demonstrate that peak metamorphic conditions were reached at around 163 Ma at c. 40 km depth in a hot subduction environment (c. 19 °C/km). U-Th-Pb zircon rim ages of 160–175 Ma obtained by Hervé and Fanning (2003) on siliceous gneisses from the Lazaro unit were interpreted as related to acidic magmatism during extension of the upper continental crust (Gondwanaland). We believe, instead, that these ages, which overlap our range, reflect zircon growth associated with the crystallization of the melt at the deep subduction interface. Temperature estimates (~750 °C) obtained for garnet amphibolite, combined with the finding of magmatic epidote and pseudomorphs after K-feldspar, confirms that metasedimentary rocks also underwent anatexis. Partial melting processes in felsic rocks triggers zircon dissolution and its subsequent precipitation during melt crystallization (Rubatto et al., 2009 and Kohn et al., 2015). Our cathodoluminescence images of zircons, together with those shown by Hervé and Fanning (2003), confirm that dissolution of detrital zircon cores most likely took place during stage 1 and associated melt production.

As also noticed by Hervé and Fanning (2003) and Willner et al. (2004a), Lazaro unit rocks have been massively affected by cooling-related metamorphic recrystallization and deformation. The stage 2 LT metamorphic event overprinting Lazaro unit rocks is characterized by growth of blue Na-rich hornblende rims around brown peak T amphibole, the formation of Si-rich phengite rims around muscovite and the pervasive replacement of garnet by chlorite. Chlorite-phengite P-T estimates show that cooling took place between 0.9 and 1.3 GPa. The formation of Si-rich phengite rims around muscovite flakes is in agreement with isobaric cooling down to 450–500 °C under epidote-blueschist facies conditions before decompression and exhumation (Fig. 15). Even though some uncertainty exists on the pressure experienced by the Lazaro unit throughout the cooling process, no significant vertical displacement can be inferred from the petrological record. In particular, the absence of orthopyroxene confirms that these rocks have not undergone near-isothermal decompression after peak metamorphism (e.g. Pattison, 2003).

An interesting feature is the observation of a low XMg garnet generation (Grt2) overgrowing the HT garnet and sealed fracture networks (Fig. 7b). Since the growth of garnet is hampered by cooling (Fig. 12), we postulate here that the pattern visible in Fig. 7b indicates (i) fracturing, breakdown and chloritization of garnet during cooling at HP (ii) short-lived warming up and healing of garnet fractures, and (iii) later cooling, fracturing and replacement by chlorite along new fracture networks. This episode of heating may be correlated with the short-lived increase of the thermal gradient from 10 to 13°/km associated with amphibolitization of the underlying Almagro blueschist complex at c. 120 Ma reported by Hyppolito et al. (2016).

Isotopic disequilibrium in Rb-Sr geochronological results independently confirms that the pervasive (but incomplete) retrogression of the Lazaro unit was a long-lasting process that took place over ca. 40 Myr between 120 and 80 Ma. Our oldest Rb-Sr age of 124 ± 27 Ma is close to the age of 117 ± 28 Ma obtained by Willner et al. (2004a) on a Lazaro unit orthogneiss (DA37) using K-Ar on amphibole and interpreted as a cooling age after HT metamorphism. These two ages suggest that the T range 550–600 °C (i.e. the assumed closure T range for K-Ar in amphibole; Villa, 1998) has been crossed at around c.120 Ma during cooling in the subduction zone environment (Fig. 15). This temperature range coincides with peak-temperatures (550–600 °C) estimated by Willner et al. (2004a, 2004b) for garnet amphibolite samples buried along a prograde metamorphic path. These garnet amphibolites (together with some retro-eclogites amphibolitized at 120 Ma from Hyppolito et al., 2016) are now exposed in the footwall of the Lazaro unit along the Puerto shear zone (Fig. 1c). This observation suggests that the Lazaro unit and the underlying garnet amphibolites from the Almagro complex probably shared a common tectono-metamorphic history since their juxtaposition at c. 120 Ma.

Last, the static sub-silicic pargasite forming over the garnet amphibolite fabric (Electronic Appendix 1; see also Willner et al., 2012 for the Choapa complex in central Chile) may be related to a later warming event, such as the emplacement of a magmatic intrusion affecting shallow levels of the wedge (<0.4 GPa), linked to the South Patagonian Batholith (e.g. Hervé et al., 2007).

8.2. Evidence for partial melting of oceanic crust

Natural occurrences exposing vestiges of subduction-related melting of oceanic crust are rare on Earth (e.g. Cuba: García-Casco et al., 2008; Catalina Schists: Sorensen and Barton, 1987; Iran: Rossetti et al., 2010). Our results provide insight on the nature of the material that experienced melting during subduction. Bulk and trace element

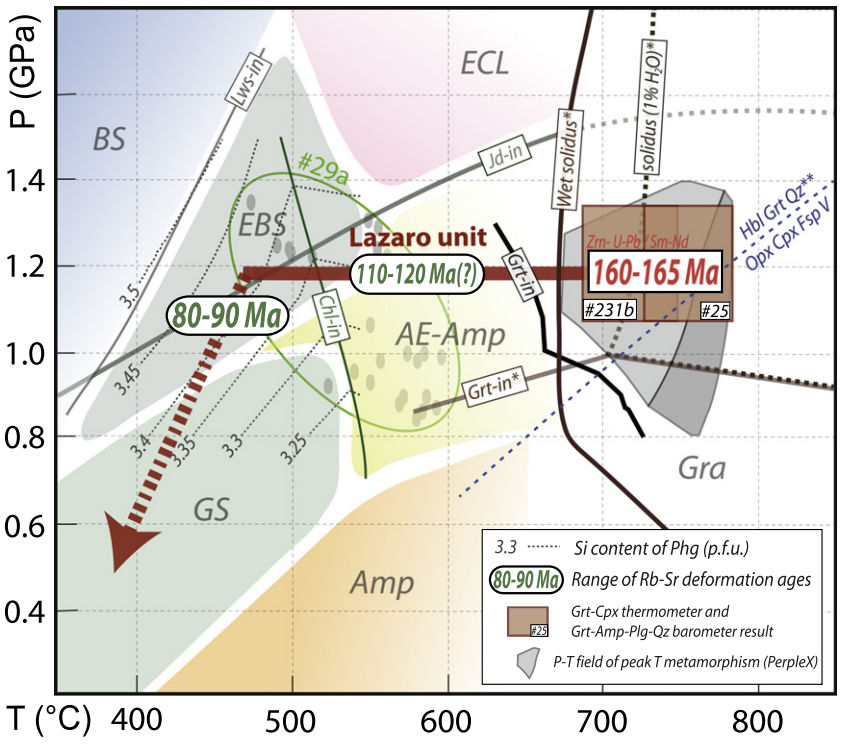

Fig. 15. Pressure-Temperature-time diagram showing the counterclockwise evolution of the Lazaro unit between 162 and 80 Ma. The garnet-in and the solidus curves are from Vielzeuf and Schmidt (2001). The (**) curve corresponding to the disappearance of orthopyroxene is from Pattison (2003). The grey-shaded domains in the peak T region correspond to the best-fit assemblage fields calculated using pseudosection modeling (Fig. 12). The red boxes correspond to P-T estimates based on conventional thermobarometry for samples #2-31b and #25 (see text and Table 3). The green circle corresponds to the best-fit ellipse for Chl-Phg P-T estimates for the LT-mylonite #29a (see Electronic Appendix 2 for details). The isopleths of the Si-contents in phengite (and the chlorite-in curve) in the epidote blueschist facies has been calculated using the bulk composition of sample #25 and a set of activity models similar to those used in Angiboust et al. (2014). The background metamorphic grid is modified after Evans (1990).

geochemical results clearly point to MORB signatures largely similar to the underlying Almagro Complex rocks (Fig. 11). The low Zr content of the trondhjemitic sample #25b (14 μg/g; Table 2) corroborates its derivation from MORB-like rocks. This also confirms that hornblende and rutile retain Zr during prograde metamorphism and melt production in mafic rocks (Kohn et al., 2015). The finding of a phengite-quartz metasedimentary rock (#24) with a detrital zircon population with ages between 1200 Ma and 280 Ma (Fig. 14) indicates that metasedimentary lenses were interleaved with mafic lithologies in the Lazaro unit. The detrital zircon pattern shows a noticeable Permian peak which is similar to those recognized in sandstones and greywackes of the Madre de Dios Accretionary Complex (MDAC; Fig. 1; Herve et al., 2003; see also Castillo et al., 2016). We do not consider these micaceous schists to derive from an upper plate granite (as proposed by Hervé and Fanning, 2003) but rather from metasedimentary rocks. In addition, the preservation of thin spessartine quartzite bands interleaved with amphibolites (Fig. 3e) supports the idea that Lazaro unit rocks correspond to a tectonic slice of ocean-floor affinity. The formation of trondhjemitic leucosomes is also a reliable indication supporting partial melting of mafic material (Fig. 10; see also Rapp et al., 1991 and Blanco-Quintero et al., 2011).

Field investigations revealed the existence of hornblende-rich amphibolites within the Lazaro unit (Fig. 3). Phase relationships and trace element patterns (Figs. 10 and 11) have shown that some of these rocks underwent melt extraction as shown by the residual geochemical signature of some samples ("picrites"; see also Fig. 11a). The large garnet crystals, however, are due to abundant water influx (Fig. 2d) confirming the residual nature of these garnet amphibolites and suggesting melt loss during stage 1 metamorphism (see also Powell and Downes, 1990). Petrological relationships and pseudosection modeling confirm that an aqueous fluid infiltrated during, and triggered, the melting process. The formation of a garnet-hornblende-bearing residue also suggests that melting proceeded before dehydration of prograde amphibolite (Figs. 3c and f; Drummond and Defant, 1990; Foley et al., 2002). The presence of 2 to 4 wt.% H_2O during the melting process (see Fig. 12) implies a contribution from external fluids since (i) high grade mafic rocks do not generally contain >1.6 wt.% H_2O (Clemens and Vielzeuf, 1987), and (ii) free fluids are needed to enable the formation of a Na-rich melt such as a trondhjemitic melt (Prouteau et al., 2001).

Hornblende-rich amphibolites and the associated garnetite domains correspond to residual solid phases and shed light on melt extraction in subduction environments (Figs. 2c and 3; Wolf and Wyllie, 1993; Sawyer, 2014). Positive volume change during melt production is known to lead to embrittlement and micro-fracturing (e.g. Connolly et al., 1997; see field evidence for micro-cracking in Electronic Appendix 1). Local melt may have collected along HT shear zones enabling melt extraction and leaving a garnetite behind (Brown, 2004). Similar garnetite has been reported by Daczko et al. (2001) in high-pressure granulites (750 °C, 1.4 GPa) from the Fjordland region (New Zealand) and by Yamamoto and Yoshino (1998) for the Jilal complex in the Kohistan arc (735–949 °C, 1.0–1.7 GPa). The generated melt escaped along these Grt-bearing restites and migrated upwards towards shallower magmatic reservoirs feeding andesitic and adakitic volcanoes (e.g. Condie, 2005; Martin et al., 2005). Therefore the Lazaro unit constitutes an interesting field analogue highlighting the nature of the source material producing Tonalitic-Trondhjemitic-Granodioritic suites (TTG) in Phanerozoic subduction zones.

8.3. A hot subduction during the Jurassic

The partial melting of the Lazaro unit took place along an 18–20 °C/km prograde thermal gradient (Fig. 15). Such a gradient is much warmer than

the one proposed for "normal" warm, present-day subduction zones where young oceanic lithosphere subducts (e.g. SW Japan: around 12°/km; Peacock and Wang, 1999). It is known that the entrance of very young oceanic lithosphere into the mantle shortly after subduction initiation can lead to very high metamorphic gradients and temperatures as high as 800 °C at 40 km depth along the interface (Defant and Drummond, 1990; Peacock, 1991; Nikolaeva et al., 2010). Numerical models confirm that after subduction initiation (typically 4–5 Ma; see Electronic Appendix 5) of an oceanic plate with a thermal age of 3 Ma, only a few millions of years are needed to reach a prograde thermal gradient of 18–20°/km. However, in the case of the south central Chile and Patagonia it is likely that subduction along the SW margin of the Gondwana continent had already started in Paleozoic times (Glodny et al., 2005; Charrier et al., 2007; Willner et al., 2009; Herve et al., 2013).

The fragmentation of the Gondwana supercontinent between middle Triassic and early Cretaceous times was characterized by an alternation of extensional regimes with subduction rate decrease and/or cessation (e.g. Gorczyk et al., 2007; Charrier et al., 2007) and synchronous extension and subduction (e.g. Stern and De Wit, 2003; Mpodozis and Ramos, 2008). Between ca. 170 and 150 Ma, extension-related intracontinental volcanic deposits covered a great part of austral Patagonia coeval with the opening of the Weddell Sea and the incipient drifting of the Antarctica Peninsula to the south (Ghidella et al., 2002; Pankhurst et al., 2000; Hervé and Fanning, 2003; Jokat et al., 2003). Our new data, in line with these models, confirm that the drift of the Antarctica Peninsula to the south, closely associated with the opening of the Weddell sea (Ghidella et al., 2002; Mpodozis and Ramos, 2008), started in the middle/late Jurassic. We hypothesize that the Lazaro unit rocks constitute remnants from hot oceanic subduction subsequently developed along the southwestern Gondwana margin in a regionally extensional regime. This late Jurassic subduction event correlates with the onset of magmatism in the forearc at c. 160 Ma when the Patagonian Batholith started to form (Hervé et al., 2007; Parada et al., 2007). An analogue of this process has been described by Kay et al. (2004) in the triple junction region (c. 49°S) where c. 12 Ma slab-melt adakites are related to the partial melting of the young and hot subducting Nazca plate (Patagonian Cordillera, Cerro Pampa). Similarly, it has been demonstrated that the SW Japanese margin evolved from a transform to a hot subduction margin over the last 30 Ma, leading to the generation of adakitic volcanoes and extension in the upper plate (e.g. Kimura et al., 2005 and references therein).

8.4. Regional implications and open questions

Diego de Almagro Island constitutes a valuable and (nearly) unique witness documenting the nature and dynamics of the South Chilean subduction zone during Mesozoic times. First, we have shown that the Lazaro unit records an early stage of accretion of hot and young oceanic crust that proceeded at c. 40 km depth along the interface (see also similar observations in E. Cuba; Blanco-Quintero et al., 2011 and Catalina island: Sorensen and Barton, 1987). Our P-T-t reconstruction suggests that the Lazaro unit (i) remained at around 40 km depth, after accretion along the hanging wall of the subduction channel, for >80 Ma (Fig. 15), and (ii) recorded the long-term thermal evolution of the Patagonian subduction zone. The time gap (160–120-80 Ma) existing between the various accreted elements on Diego de Almagro Island indicates transient episodes of underplating throughout the tectonic history of the island (e.g. Hyppolito et al., 2016; Platt, 1986; Angiboust et al., 2016).

Yet, episodes of tectonic erosion of the upper plate may have preceded or co-existed with this accretionary regime. It is striking to note the similarities between the Madre de Dios basin ages (c. 270 Ma for the youngest detrital zircons; Hervé and Fanning, 2003; Sepúlveda et al., 2010; Fig. 1c) and a marked age cluster at 270–290 Ma found in zircon cores from mica schist sample #24. From this perspective, the Lazaro unit may represent a coherent fragment of the Madre de Dios accretionary wedge consumed by tectonic erosion slightly before c. 160 Ma, followed by accretion at c. 40 km depth (see also Hervé and Fanning, 2003 and Angiboust et al., 2014).

Another similarity with previous work lies further south in the Cordillera Darwin where medium to high grade (0.9–1.2 GPa, ~620 °C) Cretaceous rocks have been described (~90 Ma to 65 Ma, ^{40}Ar-^{39}Ar cooling mica ages and U-Th-Pb on monazite; Kohn et al., 1995 and Maloney et al., 2011). Interestingly, a Jurassic Rb-Sr whole rock isochron age of 157 ± 7 Ma (Hervé et al., 1981) and an U-Pb zircon age of 164 ± 1 Ma (Mukasa and Dalziel, 1996) were obtained on a peraluminous orthogneiss from the Cordillera Darwin. It remains uncertain whether these rocks and the Lazaro unit on Diego de Almagro Island were formerly part of the same tectonic element during middle to late Mesozoic deformation along the Patagonian margin. Future investigations should help to (i) better understand the tectonic origin of the protoliths and the genesis of this cordillera and (ii) reconstruct the location of the Jurassic plate boundary and the paleogeographic link between Darwin Cordillera, Diego de Almagro and Diego Ramirez Islands (e.g. Kohn et al., 1995; Hervé et al., 2008).

Finally, the significance of the Seno Arcabuz Shear Zone, which delimits the Lazaro unit to the east, remains unclear (Fig. 1c). The fact that this shear zone was undergoing LP-HT deformation (<0.6 GPa, 500–600 °C; Willner et al., 2004a, 2004b) at c. 120 Ma while the Lazaro unit was still at HP conditions (c. 1.2 GPa; this work) needs clarification. An understanding of the evolution and significance of the Seno Arcabuz Shear Zone will be an important research target in the future as it may represent the former plate boundary prior to accretion of the Lazaro unit to the Gondwana margin.

9. Conclusions

Evidence for partial melting of subducted oceanic crust has been discovered in the Lazaro unit (Diego de Almagro Island). Thermobarometric results show that wet melting took place at around 1.2 GPa and c. 750 °C, leading to the formation of trondhjemitic melts and peritectic garnet. U-Pb dating of zircon rims and Sm-Nd geochronology on garnet-bearing HP granulite-facies assemblages reveal an age of c. 162 ± 2 Ma for this HT event. Combined with other ages showing that emplacement of the Patagonian batholith started at c. 160 Ma, we propose that the high temperature metamorphic overprint visible in the Lazaro unit records a stage of subduction of a hot and young oceanic plate along the W margin of the Gondwana continent coeval with regional extension after a period of quiescence during the Triassic. Our results also suggest that the Lazaro unit remained along the subduction interface from c. 165 Ma to 80 Ma. This long-lasting residence time explains the pervasive retrogression during isobaric cooling through epidote amphibolite and upper greenschist-facies conditions. The record of long-term deformation on Diego de Almagro Island constitutes a valuable witness to a better understanding of the structural and thermal evolution of the roots of the Chilean accretionary system from Jurassic to upper Cretaceous times.

Supplementary data to this article can be found online at http://dx.doi.org/10.1016/j.gr.2016.10.007.

Acknowledgements

Jesus Muñoz is acknowledged for field work assistance and discussions. Silvio Ferrero and Patrick O'Brien are acknowledged for insightful discussions and Philippe Yamato for sharing numerical modeling results. This project has been funded by a Deutsche Forschungsgemeinschaft (DFG) project to S.A. (AN1113-1), and São Paulo Research Foundation (FAPESP) (#2004/10203-7, #2012/01191-1) and received support for analytical costs at CIC from the University of Granada. T.H. acknowledges the grant #2014/23422-0 (FAPESP) for a post-doctoral fellowship and M.C. the Fondecyt grant #1161818. Arne Willner and Victor Ramos are fully acknowledged for insightful reviews on this manuscript. The journal editor

Damian Nance is acknowledged for his careful editorial handling. This is IPGP contribution #3794. This is IBERSIMS publication n.36.

References

Ague, J.J., Eckert, J.O., 2012. Precipitation of rutile and ilmenite needles in garnet: implications for extreme metamorphic conditions in the Acadian Orogen, USA. Am. Mineral. 97 (5–6), 840–855.

Angiboust, S., Glodny, J., Oncken, O., Chopin, C., 2014. In search of transient subduction interfaces in the Dent Blanche–Sesia Tectonic System (W. Alps). Lithos 205, 298–321.

Angiboust, S., Agard, P., Glodny, J., Omrani, J., Oncken, O., 2016. Zagros blueschists: episodic underplating and long-lived cooling of a subduction zone. Earth Planet. Sci. Lett. 443, 48–58.

Barker, F., 1979. Trondhjemite: definition, environment and hypotheses of origin. Trondhjemites, Dacites and Related Rocks 1. Elsevier, Amsterdam, p. 12.

Berman, R.G., 1991. Thermobarometry using multi-equilibrium calculations: a new technique, with petrological applications. Can. Mineral. 29 (4), 833–855.

Black, L.P., Kamo, S.L., Allen, C.M., Aleinikoff, J.A., Davis, D.W., Korsch, J.R., Foudolis, C., 2003. TEMORA 1: a new zircon standard for Phanerozoic U-Pb geochonology. Chem. Geol. 200, 155–170.

Blanco-Quintero, I.F., García-Casco, A., Gerya, T.V., 2011. Tectonic blocks in serpentinite mélange (eastern Cuba) reveal large-scale convective flow of the subduction channel. Geology 39 (1), 79–82.

Brown, M., 2004. The mechanism of melt extraction from lower continental crust of orogens. Geol. Soc. Am. Spec. Pap. 389, 35–48.

Cabanis, B., Lecolle, M., 1989. Diagrame La/10-Y/15-Nb/8: un outil pour la discrimination des series volcaniques et la mise en evidence des processus de melange et/ou de contamination crustale. Comptes Rendus de l'Académie des Sciences-Serie II 309.

Calderon, M., Prades, C.F., Herve, F., Avendaño, V., Fanning, C.M., Massonne, H.J., ... Simonetti, A., 2013. Petrological vestiges of the Late Jurassic-Early Cretaceous transition from rift to back-arc basin in southernmost Chile: new age and geochemical data from the Capitán Aracena, Carlos III, and Tortuga ophiolitic complexes. Geochem. J. 47 (2), 201–217.

Castillo, P., Fanning, C.M., Hervé, F., Lacassie, J.P., 2016. Characterisation and tracing of Permian magmatism in the south-western segment of the Gondwanan margin; U–Pb age, Lu–Hf and O isotopic compositions of detrital zircons from metasedimentary complexes of northern Antarctic Peninsula and western Patagonia. Gondwana Res. 36, 1–13.

Cesare, B., Ferrero, S., Salvioli-Mariani, E., Pedron, D., Cavallo, A., 2009. "Nanogranite" and glassy inclusions: the anatectic melt in migmatites and granulites. Geology 37 (7), 627–630.

Charrier, R., Pinto, L., Rodríguez, M.P., 2007. Tectonostratigraphic evolution of the Andean Orogen in Chile. In: Moreno, T., Gibbons, W. (Eds.), The Geology of Chile. The geological Society, pp. 21–114.

Claoue-Long, J., Compston, W., Roberts, J., Fanning, C.M., 1995. Two carboniferous ages: a comparison of SHRIMP zircon dating with conventional zircon ages & 40Ar/39Ar analysis. In: Berggren, W.A., Kent, D.V., Aubry, M.P., Hardenbol, J. (Eds.), Geochronology, Time Scales & Stratigraphic Correlation Vol. 54. SEPM Special Publication, pp. 1–22.

Clemens, J.D., Vielzeuf, D., 1987. Constraints on melting and magma production in the crust. Earth Planet. Sci. Lett. 86 (2), 287–306.

Condie, K.C., 2005. TTGs and adakites: are they both slab melts? Lithos 80 (1), 33–44.

Connolly, J.A.D., 2005. Computation of phase equilibria by linear programming: a tool for geodynamic modeling and its application to subduction zone decarbonation. Earth Planet. Sci. Lett. 236 (1), 524–541.

Connolly, J.A.D., Holness, M.B., Rubie, D.C., Rushmer, T., 1997. Reaction-induced microcracking: an experimental investigation of a mechanism for enhancing anatectic melt extraction. Geology 25 (7), 591–594.

Dale, J., Powell, R., White, R.W., Elmer, F.L., Holland, T.J.B., 2005. A thermodynamic model for Ca–Na clinoamphiboles in Na2O–CaO–FeO–MgO–Al2O3–SiO2–H2O–O for petrological calculations. J. Metamorph. Geol. 23 (8), 771–791.

Daczko, N.R., Clarke, G.L., Klepeis, K.A., 2001. Transformation of two-pyroxene hornblende granulite to garnet granulite involving simultaneous melting and fracturing of the lower crust, Fiordland, New Zealand. J. Metamorph. Geol. 19 (5), 549–562.

Defant, M.J., Drummond, M.S., 1990. Derivation of some modern arc magmas by melting of young subducted lithosphere. Nature 347 (6294), 662–665.

Drummond, M.S., Defant, M.J., 1990. A model for trondhjemite-tonalite-dacite genesis and crustal growth via slab melting: Archean to modern comparisons. J. Geophys. Res. Solid Earth 95 (B13), 21503–21521.

Dubacq, B., Vidal, O., De Andrade, V., 2010. Dehydration of dioctahedral aluminous phyllosilicates: thermodynamic modelling and implications for thermobarometric estimates. Contrib. Mineral. Petrol. 159 (2), 159–174.

Ellis, D.J., Green, D.H., 1979. An experimental study of the effect of Ca upon garnet-clinopyroxene Fe-Mg exchange equilibria. Contrib. Mineral. Petrol. 71 (1), 13–22.

Evans, B.W., 1990. Phase relations of epidote-blueschists. Lithos 25 (1), 3–23.

Foley, S., Tiepolo, M., Vannucci, R., 2002. Growth of early continental crust controlled by melting of amphibolite in subduction zones. Nature 417 (6891), 837–840.

Forsythe, R.D., Mpodozis, C., 1979. El Archipiélago Madre de Dios, Patagonia occidental, Magallanes. Aspectos generales de la estratigrafía y estructura del basamento pre-Jurásico Superior 7. Instituto de Investigaciones Geológicas, Revista Geológica de Chile, pp. 13–29.

Fuhrman, M.L., Lindsley, D.H., 1988. Ternary-feldspar modeling and thermometry. Am. Mineral. 73 (3–4), 201–215.

García-Casco, A., Lázaro, C., Rojas-Agramonte, Y., Kröner, A., Torres-Roldán, R.L., Núñez, K., ... Blanco-Quintero, I., 2008. Partial melting and counterclockwise P–T path of subducted oceanic crust (Sierra del Convento mélange, Cuba). J. Petrol. 49 (1), 129–161.

García-Casco, A., 2007. Magmatic paragonite in trondhjemites from the Sierra del Convento mélange, Cuba. Am. Mineral. 92 (7), 1232–1237.

Ghidella, M.E., Yáñez, G., LaBrecque, J.L., 2002. Revised tectonic implications for the magnetic anomalies of the western Weddell Sea. Tectonophysics 347 (1), 65–86.

Glodny, J., Kühn, A., Austrheim, H., 2008. Diffusion versus recrystallization processes in Rb–Sr geochronology: isotopic relics in eclogite facies rocks, Western Gneiss Region, Norway. Geochim. Cosmochim. Acta 72 (2), 506–525.

Glodny, J., Lohrmann, J., Echtler, H., Gräfe, K., Seifert, W., Collao, S., Figueroa, O., 2005. Internal dynamics of a paleoaccretionary wedge: insights from combined isotope tectonochronology and sandbox modelling of the South-Central Chilean forearc. Earth Planet. Sci. Lett. 231 (1), 23–39.

Gorczyk, W., Willner, A.P., Gerya, T.V., Connolly, J.A., Burg, J.P., 2007. Physical controls of magmatic productivity at Pacific-type convergent margins: numerical modelling. Phys. Earth Planet. Inter. 163 (1), 209–232.

Green, T.H., 1982. Anatexis of mafic crust and high pressure crystallization of andesite. In: Thorpe, R.S. (Ed.), Andersites. John Wiley, Chichester, pp. 465–487.

Hermann, J., Spandler, C., Hack, A., Korsakov, A.V., 2006. Aqueous fluids and hydrous melts in high-pressure and ultra-high pressure rocks: implications for element transfer in subduction zones. Lithos 92 (3), 399–417.

Hervé, F., 1988. Late Paleozoic subduction and accretion in southern Chile. Episodes 11, 183–188.

Hervé, F., Prior, D., López, G., Ramos, V.A., Rapalini, A., Thomson, S., Lacassie, J.P., Fanning, M., 1999. Mesozoic blueschists from Diego de Almagro, southern Chile. II South American Symposium on Isotope Geology, Actas, (Extended Abstract), pp. 318–321 Córdoba.

Herve, F., Fanning, C.M., Pankhurst, R.J., 2003. Detrital zircon age patterns and provenance of the metamorphic complexes of southern Chile. J. S. Am. Earth Sci. 16 (1), 107–123.

Hervé, F., Fanning, C.M., 2003. Early cretaceous subduction of continental crust at the Diego de Almagro archipelago, southern Chile. Episodes 26 (4), 285–289.

Hervé, F., Davidson, J., Godoy, E., Mpodozis, C., Covacevich, V., 1981. The late paleozoic in Chile - stratigraphy, structure and possible tectonic framework. Anais da Academia Brasileira de Ciencias 53 (2), 361–373.

Hervé, F., Pankhurst, R.J., Fanning, C.M., Calderon, M., Yaxley, G.M., 2007. The South Patagonian batholith: 150 my of granite magmatism on a plate margin. Lithos 97, 373–394.

Hervé, F., Calderón, M., Faúndez, V., 2008. The metamorphic complexes of the Patagonian and Fuegian Andes. Geol. Acta 6 (1), 43–53.

Herve, F., Calderón, M., Fanning, C.M., Pankhurst, R.J., Godoy, E., 2013. Provenance variations in the Late Paleozoic accretionary complex of central Chile as indicated by detrital zircons. Gondwana Res. 23 (3), 1122–1135.

Holland, T., Powell, R., 1996. Thermodynamics of order-disorder in minerals: II. Symmetric formalism applied to solid solutions. Am. Minerol. 81 (11–12), 1425–1437.

Holland, T.J.B., Powell, R., 1998. An internally consistent thermodynamic data set for phases of petrological interest. J. Metamorph. Geol. 16 (3), 309–343.

Holland, T., Baker, J., Powell, R., 1998. Mixing properties and activity-composition relationships of chlorites in the system MgO-FeO-Al2O3-SiO2-H2O. Eur. J. Mineral. 395–406.

Hyppolito, T., Angiboust, S., Juliani, C., Glodny, J., Garcia-Casco, A., Calderon, M., Chopin, C., 2016. Eclogite-, Amphibolite- and Blueschist-facies Rocks From Diego de Almagro Island (Patagonia): Episodic Accretion and Thermal Evolution of the Chilean Subduction Interface During the Cretaceous 264, 422–440.

Hyppolito, T., García-Casco, A., Juliani, C., Meira, V.T., Hall, C., 2014. Late Paleozoic onset of subduction and exhumation at the western margin of Gondwana (Chilenia Terrane): counterclockwise P–T paths and timing of metamorphism of deep-seated garnet–mica schist and amphibolite of Punta Sirena, Coastal Accretionary Complex, central Chile (34° S). Lithos 206, 409–434.

Inger, S., Cliff, R.A., 1994. Timing of metamorphism in the Tauern Window, Eastern Alps: Rb-Sr ages and fabric formation. J. Metamorph. Geol. 12 (5), 695–707.

Jokat, W., Boebel, T., König, M., Meyer, U., 2003. Timing and geometry of early Gondwana breakup. J. Geophys. Res. Solid Earth 108 (B9).

John, T., Gussone, N., Podladchikov, Y.Y., Bebout, G.E., Dohmen, R., Halama, R., ... Seitz, H.M., 2012. Volcanic arcs fed by rapid pulsed fluid flow through subducting slabs. Nat. Geosci. 5 (7), 489–492.

Jones, K.A., Escher, J.C., 2002. Near-isothermal decompression within a clockwise P–T evolution recorded in migmatitic mafic granulites from Clavering Ø, NE Greenland: implications for the evolution of the Caledonides. J. Metamorph. Geol. 20 (3), 365–378.

Kato, T.T., Godoy, E., 2015. Middle to late Triassic mélange exhumation along a pre-Andean transpressional fault system: coastal Chile (26°–42° S). Int. Geol. Rev. 57 (5–8), 606–628.

Kato, T.T., Sharp, W.D., Godoy, E., 2008. Inception of a Devonian subduction zone along the southwestern Gondwana margin: 40Ar-39Ar dating of eclogite-amphibolite assemblages in blueschist boulders from the Coastal Range of Chile (41 S). Can. J. Earth Sci. 45 (3), 337–351.

Kay, S.M., Gorring, M., Ramos, V.A., 2004. Magmatic sources, setting and causes of Eocene to recent Patagonian plateau magmatism (36 S to 52 S latitude). Rev. Asoc. Geol. Argent. 59 (4), 556–568.

Kimura, J.I., Stern, R.J., Yoshida, T., 2005. Reinitiation of subduction and magmatic responses in SW Japan during Neogene time. Geol. Soc. Am. Bull. 117 (7–8), 969–986.

Kohn, M.J., Spear, F.S., Harrison, T.M., Dalziel, I.W.D., 1995. 40Ar/39Ar geochronology and P-T-t paths from the Cordillera Darwin metamorphic complex, Tierra del Fuego. Chile. J. Metamorph. Geol. 13, 251–270.

Kohn, M.J., Corrie, S.L., Markley, C., 2015. The fall and rise of metamorphic zircon. Am. Mineral. 100, 897–908.

Kohn, M.J., Spear, F.S., 1990. Two new geobarometers for garnet amphibolites, with applications to southeastern Vermont. Am. Mineral. 75 (1–2), 89–96.

Lázaro, C., García-Casco, A., 2008. Geochemical and Sr–Nd isotope signatures of pristine slab melts and their residues (Sierra del Convento mélange, eastern Cuba). Chem. Geol. 255 (1), 120–133.

Leake, B.E., Woolley, A.R., Arps, C.E., Birch, W.D., Gilbert, M.C., Grice, J.D., ... Linthout, K., 1997. Report. Nomenclature of amphiboles: report of the subcommittee on amphiboles of the international mineralogical association commission on new minerals and mineral names. Mineral. Mag. 61 (2), 295–321.

Ludwig, K.R., 2009. Isoplot 4.1. A Geochronological toolkit for Microsoft Excel. 4. Berkeley Geochronology Center Special Publication, p. 76.

Maloney, K.T., Clarke, G.L., Klepeis, K.A., Fanning, C.M., Wang, W., 2011. Crustal growth during back-arc closure: cretaceous exhumation history of Cordillera Darwin, southern Patagonia. J. Metamorph. Geol. 29 (6), 649–672.

Maruyama, S., Hasegawa, A., Santosh, M., Kogiso, T., Omori, S., Nakamura, H., ... Zhao, D., 2009. The dynamics of big mantle wedge, magma factory, and metamorphic–metasomatic factory in subduction zones. Gondwana Res. 16 (3), 414–430.

Martin, H., Smithies, R.H., Rapp, R., Moyen, J.F., Champion, D., 2005. An overview of adakite, tonalite–trondhjemite–granodiorite (TTG), and sanukitoid: relationships and some implications for crustal evolution. Lithos 79 (1), 1–24.

Mpodozis, C., Ramos, V.A., 2008. Tectónica jurásica en Argentina y Chile: extensión, subducción oblicua, rifting, deriva y colisiones. Rev. Asoc. Geol. Argent. 63 (4), 481–497.
Mukasa, S.B., Dalziel, I.W., 1996. Southernmost Andes and South Georgia Island, North Scotia Ridge: zircon U-Pb and muscovite 40Ar39Ar age constraints on tectonic evolution of Southwestern Gondwanaland. J. S. Am. Earth Sci. 9 (5), 349–365.
Nikolaeva, K., Gerya, T.V., Marques, F.O., 2010. Subduction initiation at passive margins: numerical modeling. J. Geophys. Res. Solid Earth 115 (B3).
O'brien, P.J., Rötzler, J., 2003. High-pressure granulites: formation, recovery of peak conditions and implications for tectonics. J. Metamorph. Geol. 21 (1), 3–20.
O'Connor, J.T., 1965. A classification for quartz-rich igneous rocks based on feldspar ratios. US Geol. Surv. Prof. Pap. B 525, 79–84.
Olivares, B., Cembrano, J., Hervé, F., López, G., Prior, D., 2003. Geometria y cinemática de La Zona de Cizalle Seno Arcabuz, Andes patagônicos, Chile. Rev. Geol. Chile 30, 39–52.
Oncken, O., Asch, G., Haberland, C., Metchie, J., Sobolev, S., Stiller, M., ... Görze, H.J., 2003. Seismic imaging of a convergent continental margin and plateau in the central Andes (Andean Continental Research Project 1996 (ANCORP'96)). J. Geophys. Res. Solid Earth 108 (B7).
Parada, M.A., López-Escobar, L., Oliveros, V., Fuentes, F., Morata, D., et al., 2007. Andean Magmatism. In: Moreno, T., Gibson, W. (Eds.), The Geology of Chile. The Geological Society of London, pp. 115–146 (Great Britain).
Pankhurst, R.J., Riley, T.R., Fanning, C.M., Kelley, S.P., 2000. Episodic silicic volcanism in Patagonia and the Antarctic Peninsula: chronology of magmatism associated with the break-up of Gondwana. J. Petrol. 41 (5), 605–625.
Pattison, D.R.M., 2003. Petrogenetic significance of orthopyroxene-free garnet + clinopyroxene + plagioclase ± quartz-bearing metabasites with respect to the amphibolite and granulite facies. J. Metamorph. Geol. 21 (1), 21–34.
Peacock, S.M., Rushmer, T., Thompson, A.B., 1994. Partial melting of subducting oceanic crust. Earth Planet. Sci. Lett. 121 (1), 227–244.
Peacock, S.M., 1991. Numerical simulation of subduction zone pressure-temperature-time paths: constraints on fluid production and arc magmatism. Philosophical Transactions of the Royal Society of London A: Mathematical, Physical and Engineering Sciences. 335(1638), pp. 341–353.
Peacock, S.M., Wang, K., 1999. Seismic consequences of warm versus cool subduction metamorphism: examples from southwest and northeast Japan. Science 286 (5441), 937–939.
Pearce, J.A., 2008. Geochemical fingerprinting of oceanic basalts with applications to ophiolite classification and the search for Archean oceanic crust. Lithos 100 (1), 14–48.
Plank, T., Langmuir, C.H., 1993. Tracing trace elements from sediment input to volcanic output at subduction zones. Nature 362 (6422), 739–743.
Platt, J.P., 1986. Dynamics of orogenic wedges and the uplift of high-pressure metamorphic rocks. Geol. Soc. Am. Bull. 97 (9), 1037–1053.
Powell, R., Downes, J., 1990. Garnet porphyroblast-bearing leucosomes in metapelites: mechanisms, phase diagrams, and an example from Broken Hill, Australia. High-temperature Metamorphism and Crustal Anatexis. Springer, Netherlands, pp. 105–123.
Powell, R., Holland, T., 1999. Relating formulations of the thermodynamics of mineral solid solutions: activity modeling of pyroxenes, amphiboles, and micas. Am. Mineral. 84 (1–2), 1–14.
Powell, R., Holland, T., 1994. Optimal geothermometry and geobarometry. Am. Mineral. 79 (1–2), 120–133.
Prouteau, G., Scaillet, B., Pichavant, M., Maury, R., 2001. Evidence for mantle metasomatism by hydrous silicic melts derived from subducted oceanic crust. Nature 410 (6825), 197–200.
Rapp, R.P., Watson, E.B., Miller, C.F., 1991. Partial melting of amphibolite/eclogite and the origin of Archean trondhjemites and tonalites. Precambrian Res. 51 (1), 1–25.
Ravna, K., 2000. The garnet–clinopyroxene Fe^{2+}–Mg geothermometer: an updated calibration. J. Metamorph. Geol. 18 (2), 211–219.
Rossetti, F., Nasrabady, M., Vignaroli, G., Theye, T., Gerdes, A., Razavi, M.H., Vaziri, H.M., 2010. Early Cretaceous migmatitic mafic granulites from the Sabzevar range (NE Iran): implications for the closure of the Mesozoic peri-Tethyan oceans in Central Iran. Terra Nova 22 (1), 26–34.
Rubatto, D., Hermann, J., Berger, A., Engi, M., 2009. Protracted fluid-induced melting during Barrovian metamorphism in the Central Alps. Contrib. Mineral. Petrol. 158 (6), 703–722.
Sawyer, E.W., 2008. Atlas of migmatites. Canadian mineralogist special publication vol. 9. NRC Research Press.
Sawyer, E.W., 2014. The inception and growth of leucosomes: microstructure at the start of melt segregation in migmatites. J. Metamorph. Geol. 32, 695–712.
Schmidt, M.W., Poli, S., 2014. Devolatilization during subduction. In: Holland, H.D., Turekian, K.K. (Eds.), The Crust, Treatise on Geochemistry, Second Edition Elsevier-Pergamon, Oxford, pp. 669–701 4.19.
Sepúlveda, F.A., Palma-Heldt, S., Hervé, F., Fanning, M., 2010. Permian depositional age of metaturbidites of the Duque de York Complex, Southern Chile: U-Pb SHRIMP data and palynology. Andean Geol. 37, 375–397.
Shelley, D., 1967. Myrmekite and myrmekite-like intergrowths. Mineral. Mag. 36 (280), 491–503.
Smye, A.J., Greenwood, L.V., Holland, T.J.B., 2010. Garnet–chloritoid–kyanite assemblages: eclogite facies indicators of subduction constraints in orogenic belts. J. Metamorph. Geol. 28 (7), 753–768.
Snoeyenbos, D.R., Williams, M.L., Hanmer, S., 1995. Archean high-pressure metamorphism in the western Canadian Shield. Eur. J. Mineral. 1251–1272.
Sorensen, S.S., Barton, M.D., 1987. Metasomatism and partial melting in a subduction complex Catalina Schist, southern California. Geology 15 (2), 115–118.
Sorensen, S.S., 1988. Petrology of amphibolite-facies mafic and ultramafic rocks from the Catalina Schist, southern California: metasomatism and migmatization in a subduction zone metamorphic setting. J. Metamorph. Geol. 6 (4), 405–435.
Spandler, C., Pirard, C., 2013. Element recycling from subducting slabs to arc crust: a review. Lithos 170, 208–223.
Stern, R.J., 2004. Subduction initiation: spontaneous and induced. Earth Planet. Sci. Lett. 226 (3), 275–292.
Stern, C.R., De Wit, M.J., 2003. Rocas Verdes ophiolites, southernmost South America: remnants of progressive stages of development of oceanic-type crust in a continental margin back-arc basin. Geol. Soc. Lond., Spec. Publ. 218 (1), 665–683.
Sun, S.S., McDonough, W.S., 1989. Chemical and isotopic systematics of oceanic basalts: implications for mantle composition and processes. Geol. Soc. Lond., Spec. Publ. 42 (1), 313–345.
Syracuse, E.M., van Keken, P.E., Abers, G.A., 2010. The global range of subduction zone thermal models. Phys. Earth Planet. Inter. 183 (1), 73–90.
Tatsumi, Y., Eggins, S., 1995. Subduction Zone Magmatism. Vol. 1. Wiley. Frontiers in earth sciences DOI: 086542361X9780865423619.
Torres-Roldan, R.L., Garcia-Casco, A., Garcia-Sanchez, P.A., 2000. CSpace: an integrated workplace for the graphical and algebraic analysis of phase assemblages on 32-bit Wintel platforms. Comput. Geosci. 26 (7), 779–793.
Van Hunen, J., Moyen, J.F., 2012. Archean subduction: fact or fiction? Annu. Rev. Earth Planet. Sci. 40, 195–219.
Vidal, O., Parra, T., Trotet, F., 2001. A thermodynamic model for Fe-Mg aluminous chlorite using data from phase equilibrium experiments and natural pelitic assemblages in the 100 to 600C, 1 to 25 kb range. Am. J. Sci. 301 (6), 557–592.
Vielzeuf, D., Schmidt, M.W., 2001. Melting relations in hydrous systems revisited: application to metapelites, metagreywackes and metabasalts. Contrib. Mineral. Petrol. 141 (3), 251–267.
Villa, I.M., De Bièvre, P., Holden, N.E., Renne, P.R., 2015. IUPAC-IUGS recommendation on the half life of 87 Rb. Geochim. Cosmochim. Acta 164, 382–385.
Villa, I.M., 1998. Isotopic closure. Terra Nova-Oxford 10 (1), 42–47.
Walowski, K.J., Wallace, P.J., Hauri, E.H., Wada, I., Clynne, M.A., 2015. Slab melting beneath the Cascade Arc driven by dehydration of altered oceanic peridotite. Nat. Geosci. 8 (5), 404–408.
White, R.W., Powell, R., Holland, T.J.B., 2007. Progress relating to calculation of partial melting equilibria for metapelites. J. Metamorph. Geol. 25 (5), 511–527.
White, R.W., Powell, R., Holland, T.J.B., 2001. Calculation of partial melting equilibria in the system Na2O–CaO–K2O–FeO–MgO–Al2O3–SiO2–H2O (NCKFMASH). J. Metamorph. Geol. 19 (2), 139–153.
Whitney, D.L., Evans, B.W., 2010. Abbreviations for names of rock-forming minerals. Am. Mineral. 95 (1), 185.
Williams, I.S., Claesson, S., 1987. Isotopic evidence for the Precambrian provenance and Caledonian metamorphism of high grade paragneisses from the Seve Nappes, Scandinavian Caledonides. II: ion microprobe zircon U-Th-Pb. Contrib. Mineral. Petrol. 97, 205–217.
Willner, A.P., Pawlig, S., Massonne, H.J., Hervé, F., 2001. Metamorphic evolution of spessartine quartzites (coticules) in the high-pressure, low-temperature complex at Bahia Mansa, Coastal Cordillera of South-Central Chile. Can. Mineral. 39 (6), 1547–1569.
Willner, A.P., Glodny, J., Gerya, T.V., Godoy, E., Massonne, H.J., 2004a. A counterclockwise PTt path of high-pressure/low-temperature rocks from the Coastal Cordillera accretionary complex of south-central Chile: constraints for the earliest stage of subduction mass flow. Lithos 75 (3), 283–310.
Willner, A.P., Hervé, F., Thomson, S.N., Massonne, H.J., 2004b. Converging PT paths of Mesozoic HP-LT metamorphic units (Diego de Almagro Island, Southern Chile): evidence for juxtaposition during late shortening of an active continental margin. Mineral. Petrol. 81 (1–2), 43–84.
Willner, A.P., 2005. Pressure–temperature evolution of a Late Palaeozoic paired metamorphic belt in North–Central Chile (34–35 30′ S). J. Petrol. 46 (9), 1805–1833.
Willner, A.P., Sepúlveda, F.A., Hervé, F., Massonne, H.J., Sudo, M., 2009. Conditions and timing of pumpellyite–actinolite-facies metamorphism in the Early Mesozoic Frontal Accretionary Prism of the Madre de Dios Archipelago (latitude 50 20′ S; Southern Chile). J. Petrol. 50 (11), 2127–2155.
Willner, A.P., Massonne, H.J., Ring, U., Sudo, M., Thomson, S.N., 2012. P–T evolution and timing of a late Palaeozoic fore-arc system and its heterogeneous Mesozoic overprint in north-central Chile (latitudes 31–32 S). Geol. Mag. 149 (02), 177–207.
Wolf, M.B., Wyllie, P.J., 1993. Garnet growth during amphibolite anatexis: implications of a garnetiferous restite. J. Geol. 357–373.
Yamamoto, H., Yoshino, T., 1998. Superposition of replacements in the mafic granulites of the Jijal complex of the Kohistan arc, northern Pakistan: dehydration and rehydration within deep arc crust. Lithos 43 (4), 219–234.
Zen, E.A., Hammarstrom, J.M., 1984. Magmatic epidote and its petrologic significance. Geology 12 (9), 515–518.